Master's Thesis

Preparation and investigation of high entropy alloys

Ádám Vida

Materials Science MSc

Supervisor:
Lajos K Varga, Senior Research Fellow
Wigner Research Centre for Physics
Hungarian Academy of Sciences

Internal Consultant:
Nguyen Quang Chinh
Associate Professor
Eötvös Loránd University

Eötvös Loránd University
Faculty of Science

Budapest, 2015

Contents

Acknowledgments

I would like to thank

Prof. Lajos K. Varga, my supervisor, for giving me all circumstances for understanding the physics of these materials and for his endless guidelines. I greatly appreciate his supervision and trust.
Prof. Nguyen Quang Chinh, for being my co-supervisor and reading my thesis, also for a lot of experimental advice.
Péter Szommer and Dr. Péter Dusán Ispanovity, who helped me with nano indentation and for the good ideas in the explanation.
Gábor Varga, for fabrication, investigation of compressed micropillars and his good ideas while preparation the samples.
Albert Karacs, for the unique solutions during preparation of tensile test specimens and good guidelines in the field of microscopy.
Dávid S. Molnár, for his continuous support and for backing up my experimental approaches with his theoretical know-how.
Nóra Nagy and Márk Kondás, for the help in spark erosion sample production.
Ambrus Karai and János Csizmazia, who engraved the completed specimens for tensile testing.
My friends: Bálint Bertalan, Gábor Homa, Zoltán Posgay, for reading this thesis and giving good councils.
Janka Miklós-Kovács, my partner for her care and help during this year.
My family, for their support and endless love, which mean a lot to me.

Kivonat - Abstract in Hungarian

A nagyentrópiás ötvözetek (angol rövidítése HEA) a fémötvözetek új családját képezik, amelyben legalább 4 összetevő található 5-35 atomszázalékos arányban. Szemben a hagyományos ötvözetekkel, a HEA ötvözetek esetében feleslegessé válik az ötvözet alapanyaga (mátrix) és az ötvöző anyag fogalma, hiszen a nagy koncentrációk miatt nem tudunk különbséget tenni köztük. Az egyértelműség miatt ötvözeteinket az összetevők periódusos rendszerben való elhelyezkedése alapján - a külső elektronok számának fényében, csökkenő sorrendben - nevezzük el, nem pedig az alfabetikus rendet követjük.
Az irodalmi tanulmányok alapján arra a következtetésre jutottunk, hogy a HEA-k különös tulajdonságokkal rendelkeznek, melyeknek később hasznát vehetnék az ipari alkalmazásokban. A dolgozatban néhány ötvözetcsalád előállítását és mechanikai vizsgálatát mutatom be. Mintáinkat indukciós olvasztással állítottuk elő és 5 lépésben homogenizáltuk. Tipikus öntecsméretünk hossza 7 cm, átmérője 1.5 cm és tömege 25 g volt. Gyártás után a HEA ötvözeteket különböző mechanikai- és anyagparaméter-vizsgálatnak (mint mechanikai szakítóvizsgálat, sűrűségmérés, keménységmérés, röntgen diffrakció, dinamikus keménységmérés, mikroplaszticitás) vetettük alá. A kísérletileg kapott eredményeket összevetettem az első elvekből történő szimulációs eredményekkel [1].

Eredményeink arra engednek következtetni, hogy bár az ilyen összetett mikroszerkezettel rendelkező anyagcsaládok elméleti tervezése nem triviális feladat, a kutatás jó úton halad, hiszen a minták nagy részénél meglepő egyezést tapasztaltunk az elméleti és mért értékek között. A szignifikáns eltéréseket megpróbáltuk megérteni, azokra fizikai okokat keresni, majd a magyarázatokat szimulációkba ültetni az eredményesebb jóslatok megtalálása reményében.

Abstract

High Entropy Alloys (HEAs) are alloys having at least four major elements in 5-35 at.% concentration range.[1] Many studies shows that these alloys often exhibit unusual properties, which could be useful for some industrial applications. Preparation and investigation of some families of HEAs are shown in this work.[2] We have prepared our samples by induction melting in cold copper mold and homogenized them by 5 times remelting. Typical sample size and mass was $\sim$ 7 cm length, 1.5 cm diameter and 25 g, respectively. After the melting process, we have measured the density with a He pycnometer (AccuPic II 1340, USA), Vickers hardness with 1 kg load tester, dynamic hardness (UMIS CSIRO, Australia) and ultrasound propagation speed (Olympus 45 MG, Japan). We have also observed the crystalline structure and texture with scanning electron microscope (FEI Quanta 3D, USA) and made the x-ray diffraction analysis (Bruker D8). Finally we prepared micropillars from some HEAs and compressed them with the dynamic micro hardness tester, which is a novelty in the case of these types of alloys.

We have observed some crucial points from the theory of the HEAs, namely the changes in crystalline structure according to the valency electron concentration (VEC), the coctail effect, the correlation between the hardness and bulk modulus and the dendritical texture of some as-cast samples.

We compared all of our results with theoretical predictions by Dávid Molnár [1],laying on *ab initio* calculations, using the EMTO method.[3] Comparing the results we have got both negative and positive matches depending on HEA families. When we got results un-matched with the theory, we tried to understand the real behavior of these materials and to find better models for theoretical calculations.

[1]For the logical clearness we will refer our alloys by the decreasing number of valence electrons, so the alloy from aluminum, cobalt, chromium, iron and nickel is $NiCoFeCrAl$.

[2]We mean increasing atomic concentration of one element, when we are talking about family, e.g. $NiCoFeCrTi_x$, $x = 0.1, 0.2, 0.5, 1$.

[3]Our team is strongly connected to a Swedish team working in Stockholm, guided by Professor Levente Vitos.

Chapter 1

Motivation

In the classical metallurgy, conventional alloys are based on one major element (matrix) and different alloying elements are added to this system to improve some properties (hardness, ductility, resistances, etc.). We can talk about alloy families, based on one principal element, such as steel, that contains iron as a principal element and additions of several tenth percentages of carbon, manganese, chromium, nickel, tungsten, and so on. In 2004 Professor Brian Cantor and Professor Jien-Wei Yeh independently published some seminal papers [2–4] on multiprincipal alloys with nearly equiatomic (nowadays 5 to 35 at. %) compositions. Yeh named the new type of alloys as high entropy alloys (HEAs), because the large number of components increases the configuration entropy which stabilizes the simple solid solution state in melt [5]. The concept of multicomponent alloys became popular in the metallurgical society and more than 600 papers were published in this topic in the last ten years. High entropy alloys can be considered as a new class of metallic materials with a potential for use in structural applications. However, most of the studies so far have focused on microhardness and compressive strength measurements for mechanical properties determination. This study presents the tensile deformation behavior of single-phase, and double-phase HEA's together with nanointendation measurements on micropillars (first in the literature as to my knowledge).

HEAs possess high strength and hardness due to the solid solution mechanism, as well as relatively high ductility due to the crystalline structure. Elements like Cr and Al confer good corrosion and oxidation resistance [6]. Casting of HEAs can be performed by traditional metallurgical equipment, there is no need for special technologies [7]. Considering these facts, it is well founded to study these materials.

Chapter 2

Theoretical background

Taking into account the enormous number of possible compositions N, the „trial and error" investigation of new alloy composition is impossible. This number, N can be estimated taking all the possible metals from the periodic table ($C = 60$) and considering composition changes by x atomic percentage. Then one component can be changed $100/x$ times and the number of alloys for $C - 1$ independent variables would be

$$N = (100/x)^{C-1}. \tag{2.1}$$

Considering 60 elements to work with, there would be 10^{177} possibilities, for $x = 0.1\%$. By reducing the number of elements to 40 and increasing the difference to 1% in concentration percentages, there are still 10^{78} alloys (note that the number of atoms in the universe is smaller: 10^{66}) [2].
In a sharp contrast with traditional metallurgy, Cantor et al. and Yeh et al. came up with the idea of preparing equiatomic or near equiatomic compositions. They named the new family of alloys as High Entropy Alloys, because the configuration entropy is a maximum when the elements are in equiatomic proportions and this entropy contribution to Gibbs free energy stabilizes the solid solution phase.

Considering the configuration entropy of the system, the Boltzmann's equation can be used for the calculation as:

$$\Delta S_{\text{conf}} = k \ln w, \tag{2.2}$$

where k is the Boltzmann's constant and w is the multiplicity of the system. The change of (2.2) per mole for the formation of a solid solution from n elements in x_i mole fraction is

$$\Delta S_{\text{conf}} = -R \sum_{i=1}^{n} x_i \ln x_i. \tag{2.3}$$

The configuration entropy per mole for an equiatomic alloy in its liquid or regular solid solution state is [8]:

$$\Delta S_{\text{conf}} = k \ln w = -R \left(\frac{1}{n} \ln \frac{1}{n} + \frac{1}{n} \ln \frac{1}{n} + ... + \frac{1}{n} \ln \frac{1}{n} \right) = -R \ln \frac{1}{n} = R \ln n, \qquad (2.4)$$

where R is the universal gas constant, $R = 8.314 \frac{\text{J}}{\text{K mol}}$.

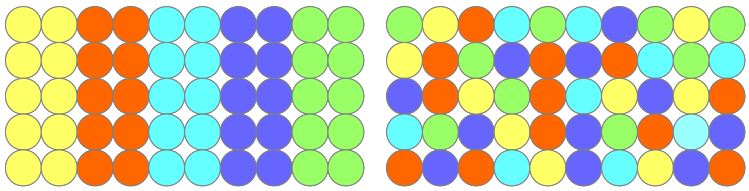

Figure 2.1: *Five component alloy with equiatomic ratios before and after mixing.*

The mixing entropy contains four contributions: the configuration, vibration, magnetic dipole and electronic randomness. From these, the configuration entropy is the dominant over the three others and the entropy increases with increasing number of elements. From Richard's rule [9, 10]:

$$\frac{\Delta H_f}{T_m} = \Delta S_f \sim R \qquad (2.5)$$

the molar entropy change (ΔS_f) from solid to liquid state during the melting process is about R and the latent heat per mole (ΔH_f) is about RT_m, where T_m is the melting temperature. The (R/mole large) mixing entropy is quite large to lower the mixing free energy (by the amount of RT) of a random solid solution. The expression of mixing free energy is:

$$\Delta G_{\text{mix}} = \Delta H_{\text{mix}} - T \Delta S_{\text{mix}}. \qquad (2.6)$$

From the uniform electron gas (UEG) theory we also know, that every mole of an ideal monoatomic gas has 1.5 RT internal energy. Because of this, such a decrease of free energy causes the phases of the solid solution to have greater chance to win against intermetallic compounds. The intermetallic compounds usually have lower configuration entropy due to the ordering. There is an upper limitation: beyond the 13 component system the growth of configuration entropy is only 0.07 R, so the practical number of elements between 4 and 13 was suggested [3].

2.1 Four core effects determining the properties of HEAs

There are several effects affecting the microstructure of HEAs, of which four are essential [11], namely the high entropy (it can interfere with complex phase transformation), severe lattice distortion (it can change the properties from the expected), sluggish diffusion (it slows down the phase transformation) and cocktail effects (it bring excess to the quantities predicted by rules of mixtures) [8, 11].

2.1.1 High entropy effect

This is the most important effect, since it enhances the formation of solid solution.The mixing enthalpy can be calculated as

$$\Delta H_{\text{mix}} = 4 \sum_{i=1, j \neq i}^{n} \Delta H_{\langle ij \rangle}^{\text{mix}} X_i X_j + \sum_{k} \Delta H_k^{\text{trans}} X_k, \tag{2.7}$$

where X_k is the mole fraction of element k and $\Delta H_{\langle ij \rangle}^{\text{mix}}$ is the mixing enthalpy of equiatomic $i-j$ alloy in the solid state. The transformation enthalpies of k-element from its standard state to metallic state are $30, 180, 310, 37, 25$ and 17 kJ/mol for *B, C, N, Si, Ge, and P*, respectively [12].
The Gibbs free energy for mixing is $\Delta G_{\text{mix}} = \Delta H_{\text{mix}} - T\Delta S_{\text{mix}}$, as prescribed in equation (2.6). Where the ΔH_{mix} and ΔS_{mix} are the enthalpy- and entropy of mixing, respectively. It can be seen, that the higher number of elements would potentially lower the mixing free energy, mainly at high temperatures with the consent of ΔS_{mix}.

According to the second law of thermodynamics, the equilibrium state has the lowest free energy of mixing in solids, although there are several possible meta-stable states. There is a competition between three possible states, namely the elemental phases, intermetallic compounds amorphous phase and solid solution phases below the lowest melting point of the alloy [11]. Elemental phase is the solid solution based on one metallic element. Intermetallic compound is a stoichiometric compound with special superlattices. Solid solution is the phase with complete mixing of all elements in a structure of body-centered cubic (BCC), face-centered cubic (FCC) or hexagonal close-packed (HCP) [13, 14].

Elemental phases have small negative ΔH_{mix} and ΔS_{mix} because of one major element. Compound phases have large negative ΔH_{mix} and small ΔS_{mix} because the ordered structure have small configuration entropy. Random solid solution phases have medium negative ΔH_{mix} (because of exist a proportion of unlike atomic pairs in solution phases) and the highest ΔS_{mix}.

Assuming that all heats of mixing for unlike atomic pairs are similar, the higher number of elements would allow the random solid solution to have the ΔH_{mix} closer to the ordered state. Because of its high ΔS_{mix} (what is lowering ΔG_{mix}), random solid solution state is more favorable in thermal stability than ordered state. In reality it is not an absolutely correct statement, that all the mixing heats for unlike atoms are equal. We can say that partially ordered solid solution phases having multicomponent composition and a certain degree of disorder instead of stoichiometric compounds are favorable at equilibrium [5]. This tendency is much stronger at high temperatures because of the $-T\Delta S_{\text{mix}}$ term.

The stability of random solid solution phases is affected also by the atomic size differences among the elements in the HEA. A large difference would cause the lattice to be heavily distorted adding strain energy to ΔH_{mix}, thus to ΔG_{mix}. It is well known, that the atomic size difference is one of the main factors which determines the microstructure [15–18].

For theoretical ab initio calculations, only simple, one - phase solid solution alloys can be taken into account. For practical applications however, many HEAs with two phases are useful and have great potential.

2.1.2 Severe lattice distortion effect

Because of near equiatomic concentrations, we can not speak about matrix and solute atoms, each atom is surrounded by different kinds of atoms. This structure suffers from strains and stresses, mainly because of differing atomic sizes, illustrating in Fig. 2.2.

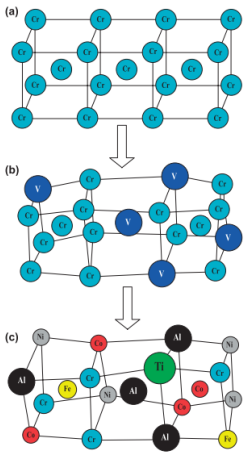

Figure 2.2: *Diagram showing lattice distortion in 5 component BCC lattice.*

Lattice distortion affects various properties and reduces the thermal effect on properties. Strength and hardness effectively increase because of solid solution hardening in the distorted lattice. For example, it is known from the literature [19, 33] that hardness value of refractory BCC equiatomic alloy MoNbTaVW is 5250 MPa which is three times higher than obtained by the mixture rule. FCC materials show much lower solid solution hardening than BCCs. The reason can be that the FCC lattice has 12 nearest neighbors and the BCC has only 8. For the same set of elements, FCC lattice has smaller fraction of unlike atomic pairs and smaller distortion strain and solution hardening than BCC lattice.

2.1.3 Sluggish diffusion effect

In a phase transformation, that is diffusion-controlled, the formation of a new phase requires cooperative movement of many different kinds of atoms. As it has been explained in the previous section, a HEA mainly contains lots random and ordered solid solutions. The diffusion of an atom in the whole-solute matrix would be different from the conventional alloys. A vacancy in the whole-solute matrix may be surrounded and competed by totally different atoms. Higher activation energy and slower diffusion is expected due to the large fluctuations of lattice potential energy [20].

The sluggish diffusion has also effect on phase nucleation, phase growth and distribution. The slow kinetics in HEAs allows the supersaturated state and nano-precipitates in the as-cast state also [21, 30, 31]. Because of this, HEAs could be used as diffusion barrier coatings [26, 37].

2.1.4 Cocktail effects

In a HEA we can find one, two or more phases, depending on the composition and the processing. The properties of the sample originate from the individual phases, including the phase size, boundaries, distribution and properties of every single phase. Moreover, every phase could be regarded as atomic scale composites, so the prediction of average behavior is not so easy, the composite properties not only come from mixture rules, but also from mutual interactions.

Yeh showed the cocktail effect introduced by the interaction of constituent elements in the $Al_xCoCrCuFeAl$ alloy, which leads to a phase transformation from an FCC structure to a BCC when the Al content is increased beyond critical value, as shown on Fig. 2.3. [8].

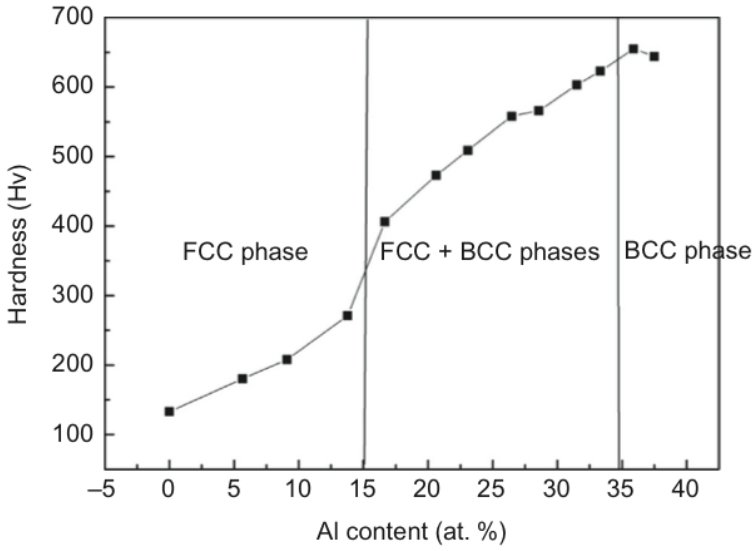

Figure 2.3: *Cocktail effect introduced by the interaction of constituent elements in the $Al_xCoCrCuFeAl$ alloy - from the article [8].*

2.2 Crystal structure of Simple Solid Solution phases

The is an important question: what will the crystalline structure be, if an HEA crystallizes into simple phases? Virtually all simple solid solution phase have either FCC, HCP and BCC structure [19, 22, 32, 34, 35].

It seems that the most critical factor that decides the establishment of FCC or BCC structure is the valence electron concentration (VEC). This is calculated from the weighted average of each element's VEC. Guo et al. found that when VEC is larger than 8, FCC phase is the stable. Also when it is smaller than 6.87, the BCC structure stabilizes. In the interval from 6.87 to 8 in VEC, both phases are observed [35]. The mechanism is not fully understood.
The as-cast state is typically not in thermodynamic equilibrium. Guo found, that alloys in stabilized FCC or BCC state regions are not so disturbed in higher temperatures, where phase transformation is less significant. However this is not true for elements in the mixed region, there the phase transformation will play a key role.

Chapter 3

Experimental methods

Whereas we obtained atomic concentrations from theoretical calculations [1], we prepared the alloys from pure metals with high precision. We used induction melting in cold copper mold with protective argon atmosphere to prepare our specimens. Protective atmosphere is important to prevent oxidation and loss while homogenizing the solid solutions. Every ingot was at least five times re-melted to help the work of diffusion in homogenising. Let's see the techniques in-detail.

3.1 Induction melting

This kind of melting is based on the periodical change of an electromagnetic field near to the sample. The changing magnetic field causes eddy current, which produces heat. The available temperature is given by the backfill and the material quality. The induction heating is also a good choose, because the eddy currents are mixing the melt and this is also a good point at homogenisation. Main parts of the device are shown schematically in Fig. 3.1.

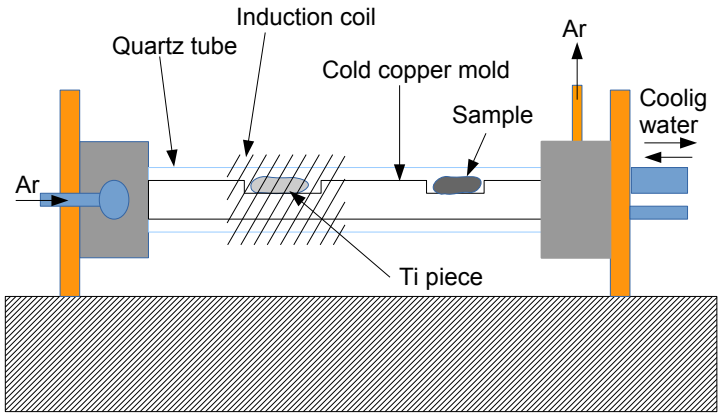

Figure 3.1: *Scheme of induction melting.*

The generator was manufactured in Czechoslovakia in the 70's and it was renovated in 2008. From this year, the available frequency is 1 GHz. The high frequency feed out is focused in 7 cm-s region of the cooled copper mold and there is a quartz tube with a bigger diameter thereon. Between the two tubes there is a protective argon atmosphere, which is injected from the left side and it goes out in the right side, front of the machine. After inserting the pieces of pure metals (or the sample in the case of remelting) we rinsed it for 5 minutes with argon, then we heated up the titanium piece to catch the possibly stuck oxygen molecules.
With screw mechanics we could move the induction coil in horizontal direction from the titanium piece to our sample, that was the way to start the melting process.
Typical mass of specimens were between 15-25 grams (this is the easy size to work with). Their length and diameter is dependent on atomic composition and it is controlled by the surface tension of the melt, but a typical length was around 7 cm with a diameter of 1.5 cm.

3.2 Ultrasonic testing

This is a relatively new technique to estimate some physical characteristics of materials. The sound propagation in metals is in connection with elastic constants like Young's modulus (E), bulk modulus (B) and shear modulus (G). The concrete expressions are

$$G = \rho \cdot v_t^2 \tag{3.1}$$

$$E = G \cdot \frac{3v_l^2 - 4v_t^2}{v_l^2 - v_t^2} \tag{3.2}$$

$$B = \rho \cdot \left(v_l^2 - \frac{4}{3} v_t^2 \right), \tag{3.3}$$

where v_l is longitudinal and v_t is the transversal sound speed (in $\frac{m}{s}$), ρ is the density (in $\frac{kg}{m^3}$) of the material. It is not a trivial task to do the measurement, we had to find a device that could be used for this project. We have used Olympus 45 MG, that is a wall thickness tester and it is capable to measure sound propagation if we know the thickness precisely (in a laboratory environment, this is not a big problem). The device is able to generate and detect shear and longitudinal waves by changing the transducer.

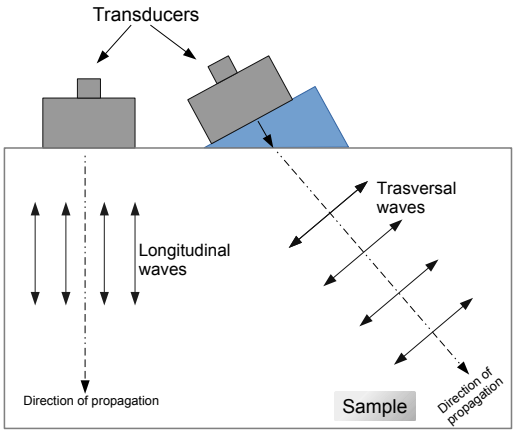

Figure 3.2: *Ultrasonic waves in materials.*

Since the diameter of transducers were only 5 mm, we could easily to measure the velocities. in order to obtain good results, we did 5 measurements in every sample and calculated their average. This is an important process, because the waves can diffract on defects.

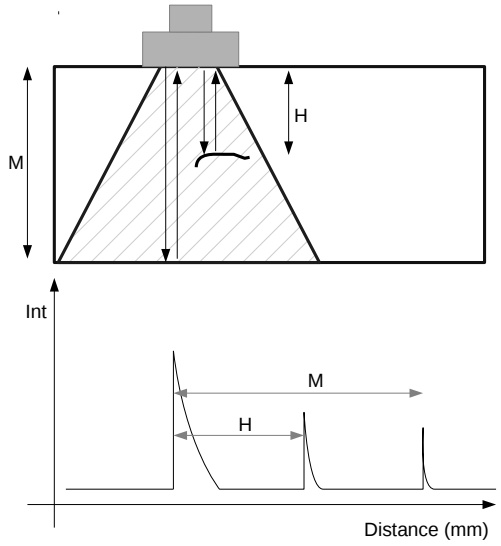

Figure 3.3: *Sound propagation in common material.*

The second important thing was the parallelism of two opposite faces, so we polished our samples to parallel at metallography laboratory at Department of Materials Physics, Eötvös University (ELTE).

3.3 Hardness testing

Hardness is the measure of a solid matter's resistance against any kinds of shape change, when compressive force is applied. There are many classification of hardness testing. In our case the importance is on Vickers hardness. This is an indentation technique, where the indenter (a diamond in the form of a square-based pyramid) is much more harder then the investigated material.

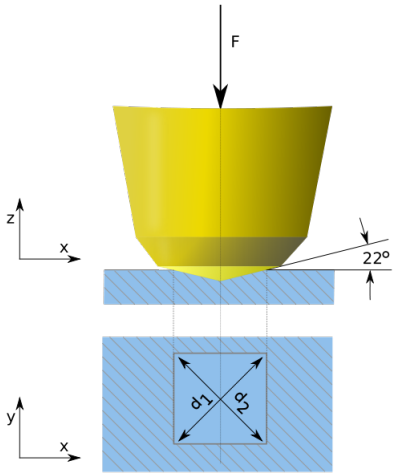

Figure 3.4: *Geometry of Vickers indenter standard.*

The surface softness is the crucial point of the measurement, since the evaluation starts with obtaining the two diameters of the indentation mark, so the smooth surface reduces the error of hardness values. We measured these lengths with built-in microscope. Common definition of Vickers hardness is the following

$$HV = \frac{F}{A} \approx \frac{1.8544F}{d^2}, \tag{3.4}$$

where F is in kgf and d is in millimeters. To calculate Vickers hardness in SI units, we have to convert kilogram-force to newtons, by multiplying with standard gravity ($g \approx 9.81 \frac{m}{s^2}$ in Budapest) and dividing by 1000 to get result in GPa. To do this calculation instantly, we can use the following expression

$$HV = \frac{F}{A} \approx \frac{0.1891F}{d^2}, \tag{3.5}$$

where F is in newtons and d in millimeters.

3.4 Micropillar fabrication and indentation

Studies suggest, that plastic behavior may change significantly in micrometers scale [49]. Specimens cannot be considered as infinite in size, the dislocations (which are responsible for plastic deformations) can sense the boundaries, so they are limited in movement. In this case we have to fabricate new theories, which take also the size effects into account. Up to our knowledge the alloys presented in this thesis have not been investigated

by micropillar tensile testing so far, this kind of investigation is step froward in the topic.

We prepared (by cutting and polishing) our as-cast samples at ELTE, in the Research and Instrument Core Facility and fabricated the pillars by focused ion beam installed to Quanta FEI 3D scanning electron microscope (SEM). Three pillars were placed on a previously selected area. Their typical height was $\sim 10\mu m$ and diameter $\sim 3\mu m$.

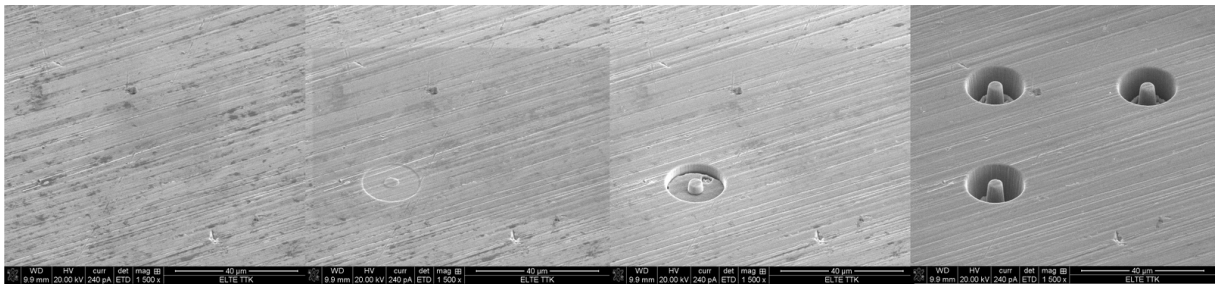

Figure 3.5: *Work process of micropillar fabrication in NiCoFeCrMn sample.*

We performed dynamic hardness test after the fabrication with flat-ended conical diamond indenter, as shown schematically in Fig. 3.6.

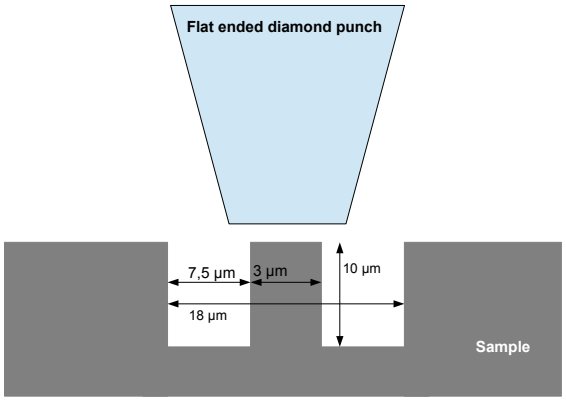

Figure 3.6: *Schematics for micropillar compression.*

We recorded the force and displacement data by micro hardness tester (UMIS CSIRO, Australia) and after testing we took back our samples to the SEM to examine the plastic deformations, the surface morphology of the compressed pillars.

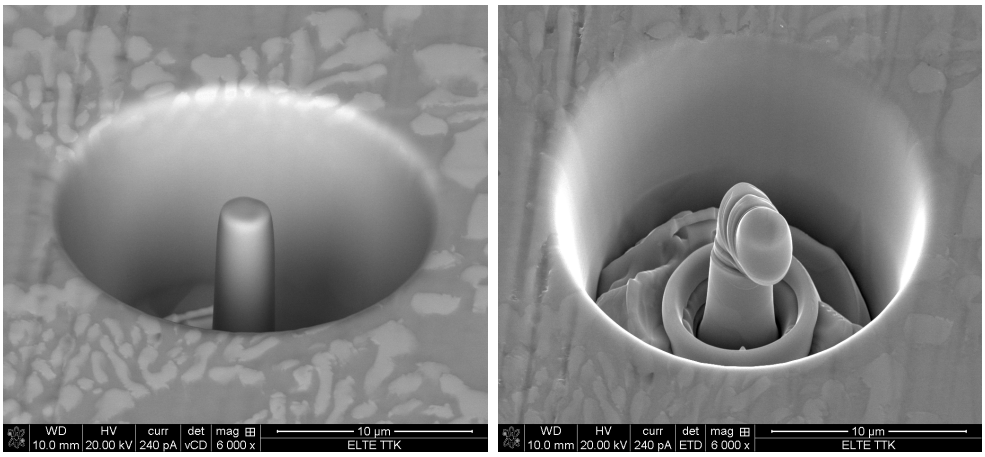

Figure 3.7: *Freshly fabricated and indented micropillar of* $Ni_{35}Fe_{30}Cr_{20}Mo_{10}W_5$.

3.5 Density measurement

When characterizing the alloys, it is important to know the precise densities. We have used He gas pycnometer (Accupic 1340, United States) in our investigation. This device can be used to measure the volume of random shaped samples and combined with analytic mass measurements, we can obtain the density (the machine calculates it automatically).

3.6 Tensile test

Tensile test is a fundamental materials science test, the sample is exposed to controlled tension until the failure. This is the way to check and to predict the materials behavior, how it will react under different types of forces. The directly measurable properties are the ultimate tensile stress (the maximum stress, that a material can withstand before breaking), the maximum elongation and reduction in area. From these measurements we can determine: Young's modulus, Poisson's ratio, yield strength and strain-hardening characteristics [50].

To obtain trustworthy results, we had to use a standardized cross-section sample. Our as-cast samples were smaller than the common standard, so we had to reduce it in size. Our sample is shown in Fig. 3.8.

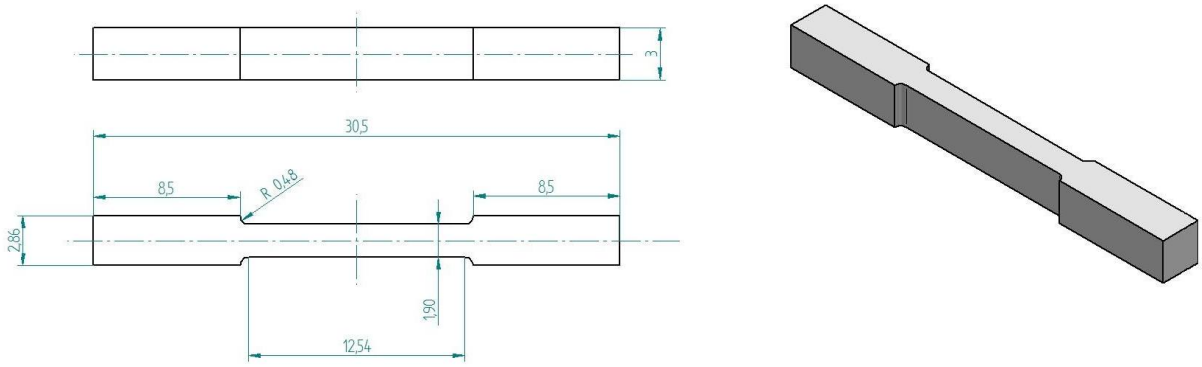

Figure 3.8: *Schematics of sample cross-section. All the parameters are in mm.*

For the evaluation of such type of investigation we have to know the elongation and the cross section of the specimen. Our device was capable of measuring the force along the process, to obtain the elongation we used the classic method: we engraved 10 marks to similar distances to the standards by laser technique with nm accuracy. In the Fig. 3.9 we can see a typical specimen before and after the tensile test.

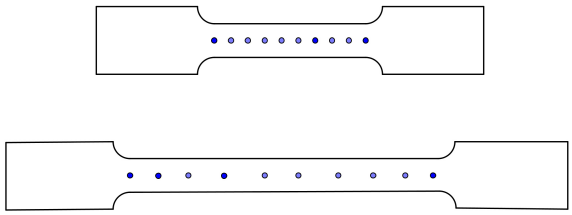

Figure 3.9: *Schematics of sample before and after the extension. We can conclude the elongation from the increasing distance of markers.*

We determined the sample elongation by digital microscope and PC software with an accuracy of 0.01 mm. In accordance with this, we can evaluate the engineering stress (σ) and strain (ε) as:

$$\sigma = \frac{F}{A_0} \text{ and } \varepsilon = \frac{\Delta l}{l_0} \tag{3.6}$$

where Δl is the change in gauge length and l_0 is the initial gauge length. If we want to calculate the true stress and strain curves, we should use the elongation and cross section values in the moment of rupture, so

$$\sigma' = \frac{F}{A} \text{ and } \varepsilon' = \ln \frac{l}{l_0} = \ln \left(1 + \frac{\Delta l}{l_0}\right) \tag{3.7}$$

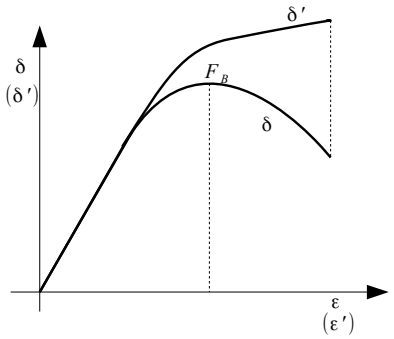

Figure 3.10: *Engineering and true stress-strain curve.*

3.7 X-ray crystallography

X-ray crystallography is a technique that can be used to identify the structure of crystals. The atoms or molecules of the crystal cause a beam of X-rays to diffract into specific directions. Atoms scatter X-ray waves primarily through the electrons and this process produces secondary spherical waves spreading from electrons. This is the so called elastic scattering. These waves cancel each other in most directions trough destructive interference and constructively in some directions, which are determined by Bragg's law

$$2d \sin \Theta = n\lambda, \tag{3.8}$$

where d is the distance between the crystal planes, Θ is the incident angle, n is an integer and λ is the wavelength of the X-ray beam.
X-rays are an optimal choice to produce the diffraction because their wavelength is typically the same order ($\sim 1 - 100$ Å) as the spacing d between planes in the crystal.

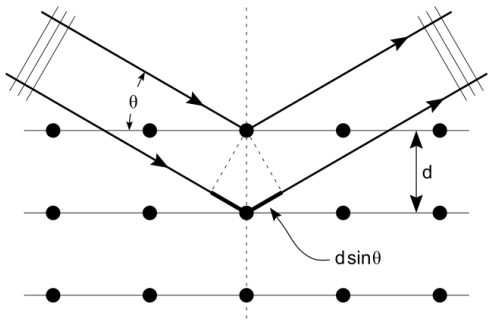

Figure 3.11: Schematics of Bragg reflection [52].

Chapter 4

Results and discussion

For the better review, I will group our samples by their families. In the frame of this thesis, we have produced 23 compositions, held together by 4 families, namely the:

- **Stainless steel based HEAs**, consisting of Ni, Co, Fe, Cr base and having one element of $Al, Ga, Sn,$ or Ge.
- **Titanium family** where the base is Cu, Ni, Co, Fe, Cr and there is titanium in increasing atomic concentration.
- **Aluminum family** where also Ni, Co, Fe, Cr base and increasing atomic concentration of aluminum can be found.
- **Refractory HEAs** containing Ni, Fe, Cr, Mo, W in different atomic percentages.

In the next sessions I will present the experimental results and their discussions from family to family.

4.1 Stainless steel based HEAs

Composition	Code	Calculated density $[g/cm^3]$	Experimental density $[g/cm^3]$
$NiCoFeCrAl$	rm1	6,724	7,0169
$NiCoFeCrGa$	rm2	no data	8,2000
$NiCoFeCrSn$	rm3	no data	8,3430
$NiCoFeCrGe$	rm4	no data	8,2100
$NiCoFeCr$	rmr	8,1822	8,3909

Table 4.1: *Atomic percentages, code names and densities of stainless steel HEAs. Some calculated densities are missing. The calculation method goes wrong with some elements, like Ga, Sn, Ge [1].*

When we measured the microhardness of samples, we obtained two average values (in gaussian distribution) for the two phased materials.[1] Let us introduce the summary of these measurements. We will show the specific measured data per family.

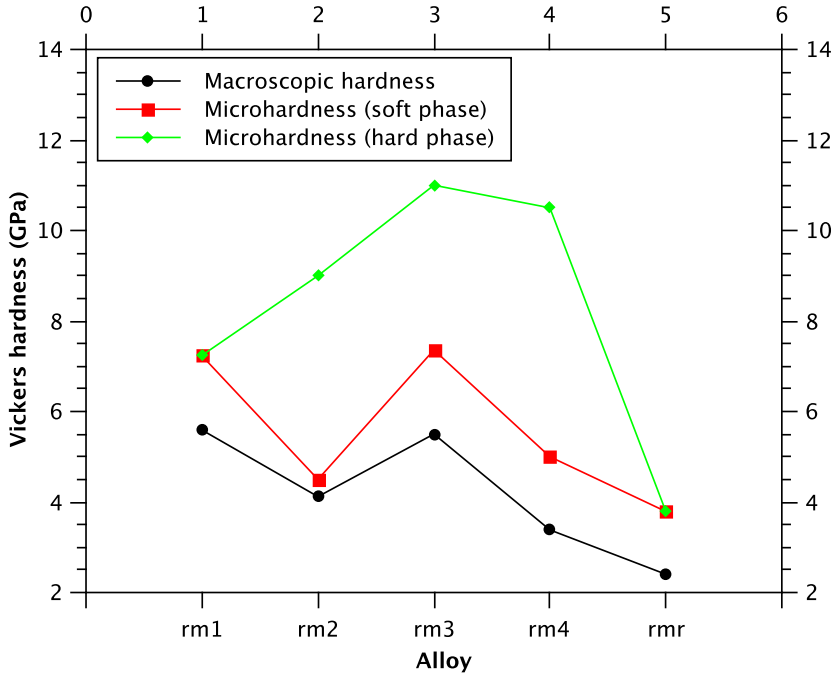

Figure 4.1: *Comparing the micro- and macroscopic hardness values of stainless steel based HEAs.*

[1]In the case of microhardness measurements the maximum load was 50 mN and the diameter of the indentation around 2 μm, furthermore in the case of macro measurements, the maximum load was 10N and the diameter of indentation $\approx 100\mu m$. Considering this, it can be stated, that the microhardness testing provides result from only one phase.

It can be seen (Fig. 4.1) that macroscopic hardness value has same trend like the microscopic value of softer phase. Therefore, we will use the lower value in the future. We compared the Vickers hardness and the VEC (Fig. 4.2).

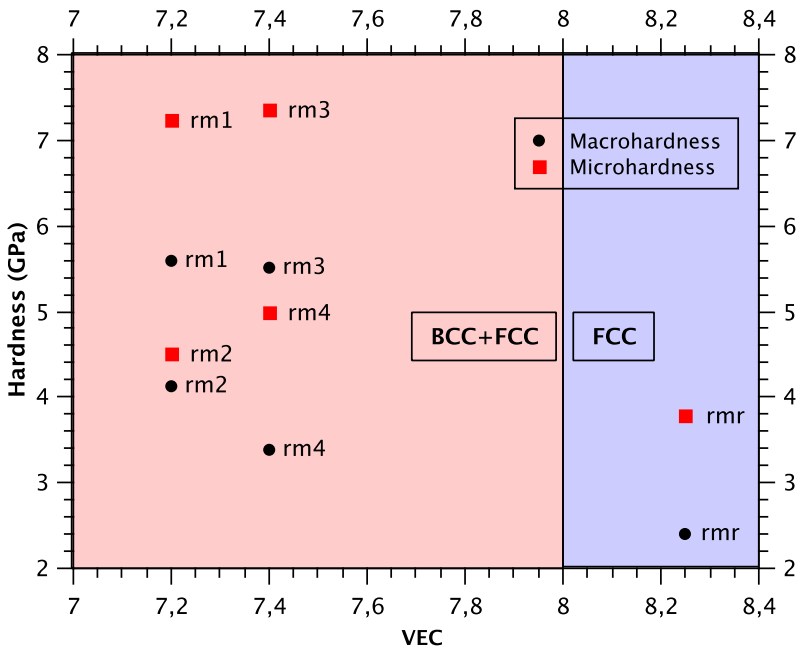

Figure 4.2: *Comparison of VEC and Vickers hardness. As we mentioned in the theoretical introduction, there is a guideline, what suggests that under the VEC value 8 there is FCC/BCC mixture and from 8, true FCC phase is expected.*

Considering this result, we wanted to be sure, that alloy *rmr,* which is the reference alloy ($NiCoFeCr$) of this family is one phased (since this is the only one in the FCC region of VEC). Furthermore, as we can see, the hardness value is decreasing with increasing valence electron concentrations, since the BCC materials are more brittle than FCC, their hardness is also higher. Let us introduce the results obtained from SEM investigation.

4.1.1 Alloy: rmr (Ni,Co,Fe,Cr)

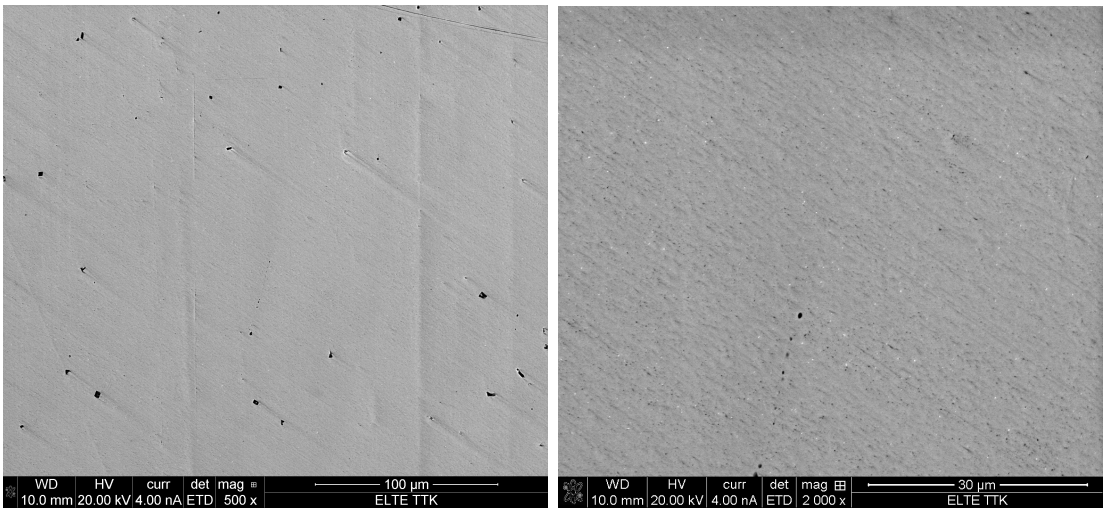

(a) 500x magnification. **(b)** 2000x magnification.

Figure 4.3: *SEM pictures of alloy rmr.*

One of the most important tasks was to get evidence, that the alloy contains only one phase, or not. Even though the SEM picture (Fig. 4.3) do not show any decomposition, we prepared the element map (with Energy-Dispersive X-Ray Spectroscopy (EDS)) from this sample also. The result can be seen in Fig. 4.4.

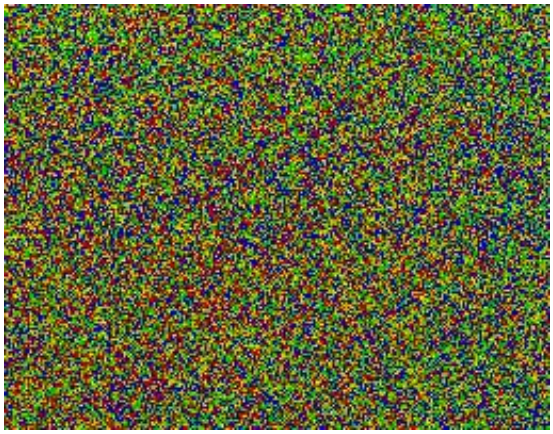

Figure 4.4: *Map of elements of alloy rmr. Each color belongs to local maximum intensity of pure elements, more precisely: red = chromium, green = iron, blue = cobalt, yellow = nickel. It can be stated, that sample contains only one phase.*

Based on the element map, there is any grouping of atoms in the investigated area. As we waited, the result of nanoindentation measurements were satisfactory, there were only one hardness value of the sample.

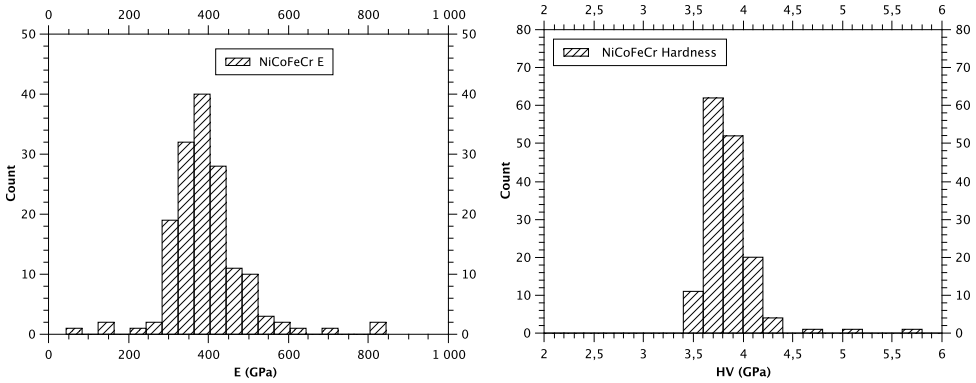

(a) Young's modulus from nanoindentation.

(b) Nano hardness from nanoindentation.

Figure 4.5: *Young's modulus and Nano hardness values from 400 Dynamic Hardness Measurements from* (200×200) μm *region, sample rmr.*

4.1.2 Alloy: rm1 (Ni,Co,Fe,Cr,Al)

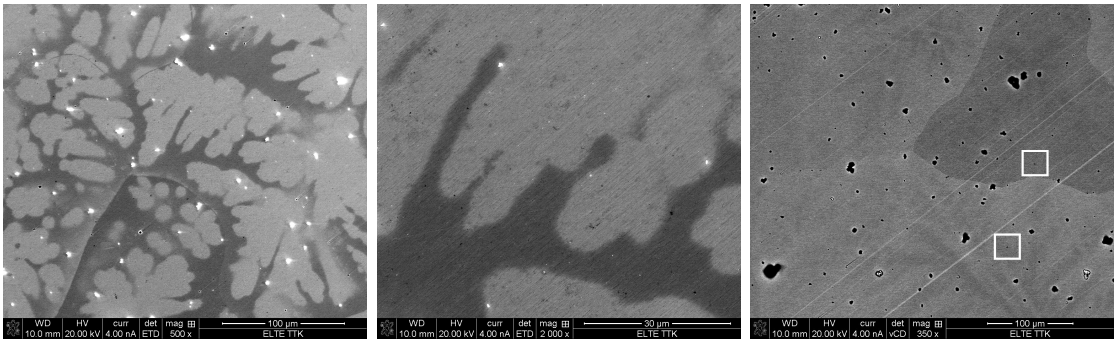

(a) Surface of rm1 (scale bar, 100 μm).

(b) Two phases of rm1 (scale bar, 30 μm).

(c) Sampling range (scale bar, 100 μm).

Figure 4.6: *Snapshots of the surface of rm1 (Ni,Co,Fe,Cr,Al). In the picture (c) we can see the localization of XRD element analysis. The bright spots in picture (a) are the remaining AlO pieces from polishing.*

The result of the element analysis is the following:

Element	Dark [At%]	Light [At%]
Al	18,34	22,05
Cr	21,97	18,85
Fe	21,21	19,44
Co	19,89	19,88
Ni	18,69	19,78
Total	100	100

Table 4.2: *XRD analysis of the sample rm1.*

It can be seen from Tab. 4.2 that the aluminum and chromium concentration changed significantly between two phases. The VECs for decomposition phases are $7,24$ for dark and $7,12$ for light areas. According to this, there is no significant phase difference between them, rather, there is an interesting fine structure (Fig. 4.7).

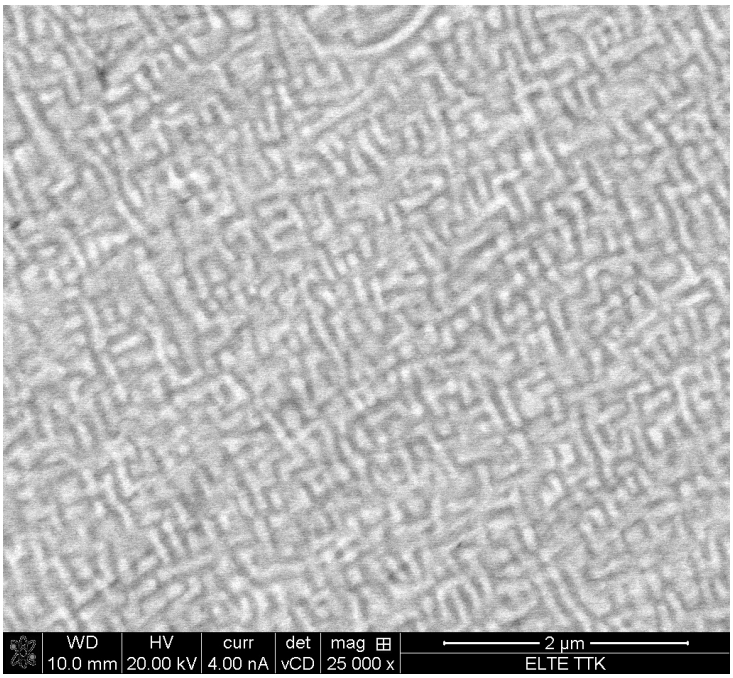

Figure 4.7: *Fine structure on alloy rm1, light region.*

The structure is similar to that of in $AlMo_{0.5}NbTa_{0.5}TiZr$ alloy [45] with two bcc phases, or to that having coherent mixtures of BCC/B2 phases in $AlCoCrCuFeNi$ [46].

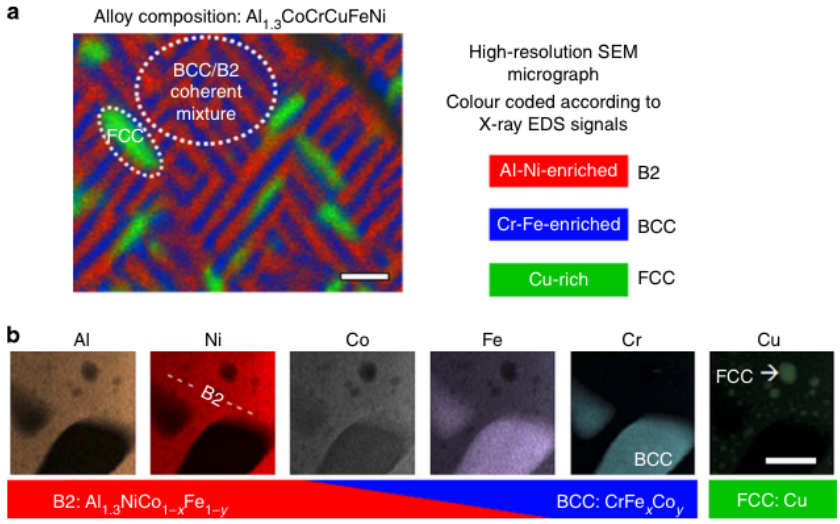

Microscopy and elemental analyses. (**a**) The high-resolution SEM micrograph is colour coded according to EDS, highlighting how the elements segregate and enrich the room temperature phases (B2, BCC and FCC). Scale bar, 0.5 µm. (**b**) The abundance of each individual element is shown in a series of TEM/EDS images of the same sample region. The selected sample area includes a contiguous B2 region, with two rectangular (roughly) BCC phases, at the bottom and left side, and smaller circular FCC nanopreciptitates. The EDS reveals that Al and Ni are nearly exclusive to the B2 phase (that is, the other regions appear black), Co and Fe are present in both the B2 and BCC phases and Cr is nearly exclusive to the BCC phase. Cu is found nearly exclusively in the nanopreciptitates, which are FCC or ordered variants. The larger FCC interdendritic regions and rod-shaped precipitates, not shown here, also contain mostly Cu. Scale bar, 0.1 µm.

Figure 4.8: *The fine structure from [46].*

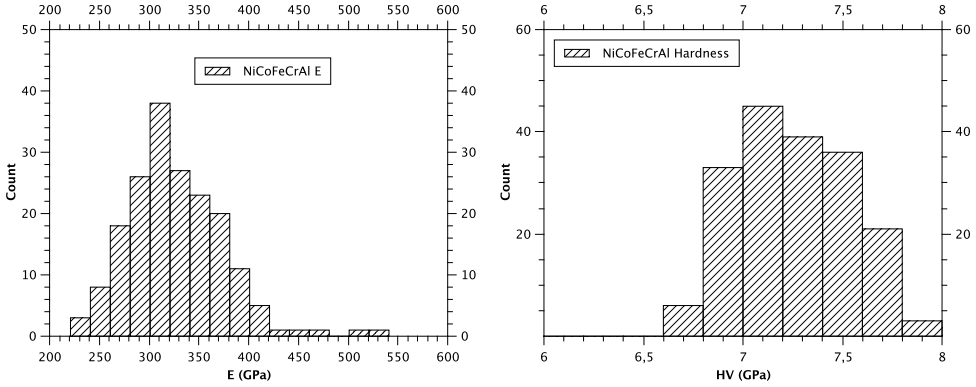

(a) Young's modulus from nanoindentation.

(b) Nano hardness from nanoindentation.

Figure 4.9: *Young's modulus and Nano hardness values from 400 Dynamic Hardness Measurements from* (200×200) *μm region, sample $rm1$.*

Based on the nanoindentation measurements, the is no significant difference in the hardness value of the two phases (Fig. 4.9).

4.1.3 Alloy rm2 (Ni,Co,Fe,Cr,Ga)

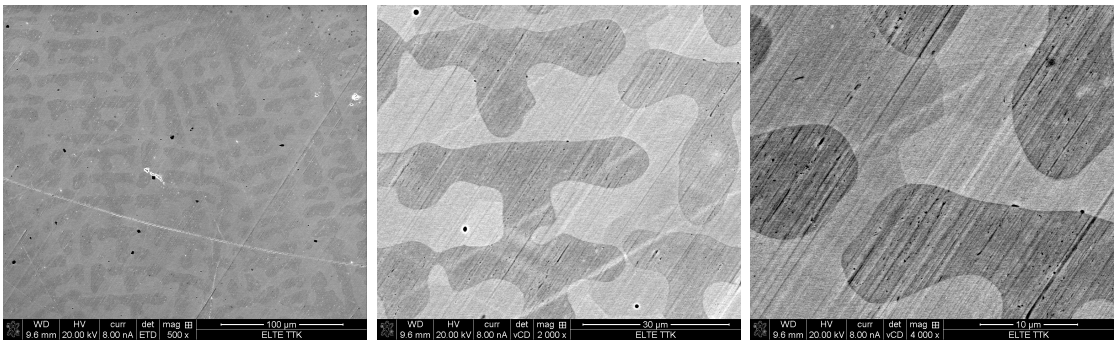

(a) Surface of rm2 (scale bar, 100 μm).

(b) Phases of rm2 (scale bar, 30 μm).

(c) Three phases of rm2 (scale bar, 10 μm).

Figure 4.10: *Snapshots of the surface of rm2 (Ni,Co,Fe,Cr,Ga).*

To obtain the composition of the phases, we collected the x-ray photons caused by electrons to do some element analysis.

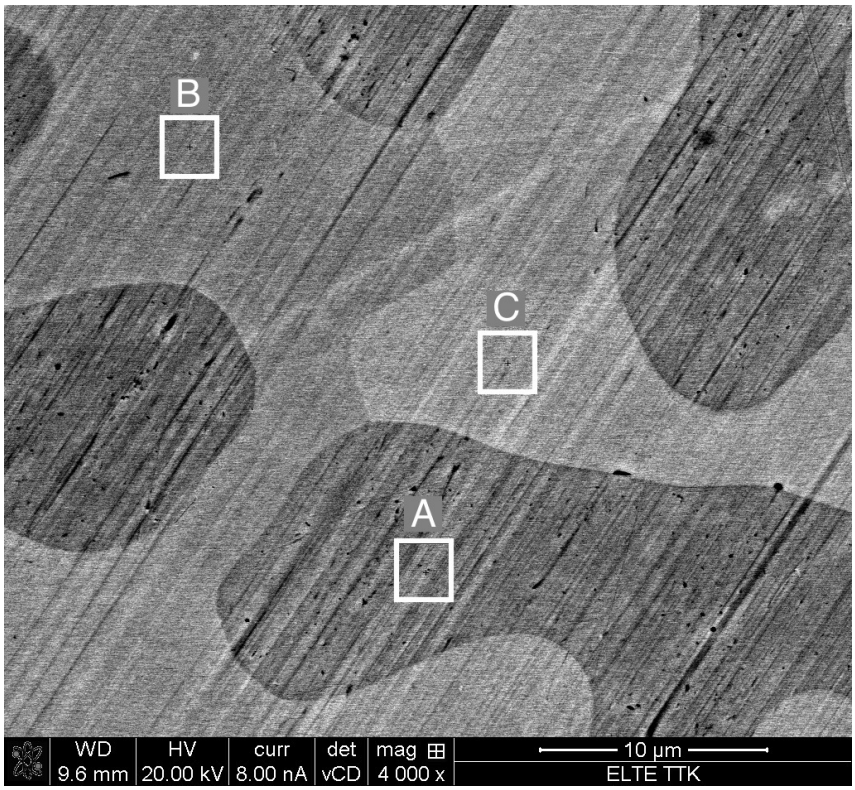

Figure 4.11: *Sampling spots of rm2.*

The results are listed below:

Element	**Region A [At%]**	**Region B [At%]**	**Region C [At%]**
Crl	22,31	18,88	18,70
Fe	23,13	17,90	17,73
Co	21,44	17,90	17,76
Ni	17,47	21,77	21,95
Ga	15,66	23,56	23,85
Total	100	100	100

Table 4.3: *XRD analysis of the sample rm2.*

It can be seen that, the B and C phases are almost the same, so material can be considered to be a two-phase alloy. The first phase is rich in chromium, iron and cobalt, but weak in nickel and gallium and the other phase is the opposite. The three „colors" can be caused by different grain orientation. The VEC of **A** phase is 7,32, for the **B** and **C** phase is 7,12. These values are in the region of FCC/BCC mixture.

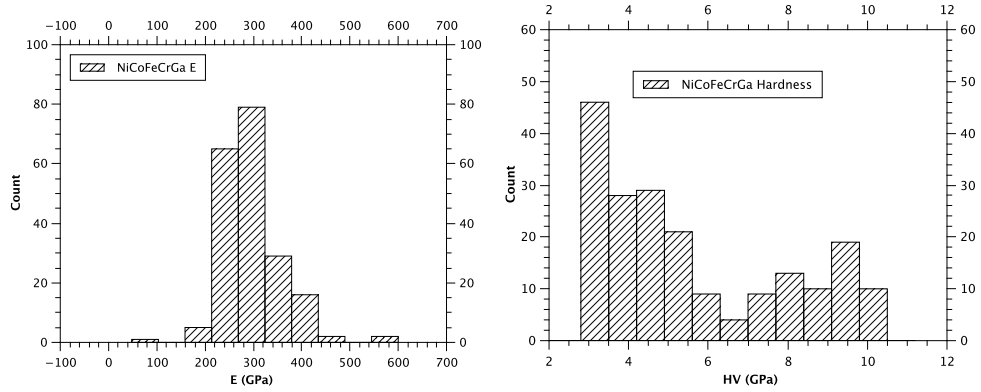

(a) Young's modulus from nanoindentation. **(b)** Nano hardness from nanoindentation.

Figure 4.12: *Young's modulus and Nano hardness values from 400 Dynamic Hardness Measurements from* (200×200) *μm region, sample rm2 (Ni,Co,Fe,Cr,Ga).*

In the Fig. 4.12 we can see different hardness values. The difference is high enough, almost 6 GPa, more investigation is needed to obtain the crystal structure of the harder phase.

4.1.4 Alloy rm3 (Ni,Co,Fe,Cr,Sn)

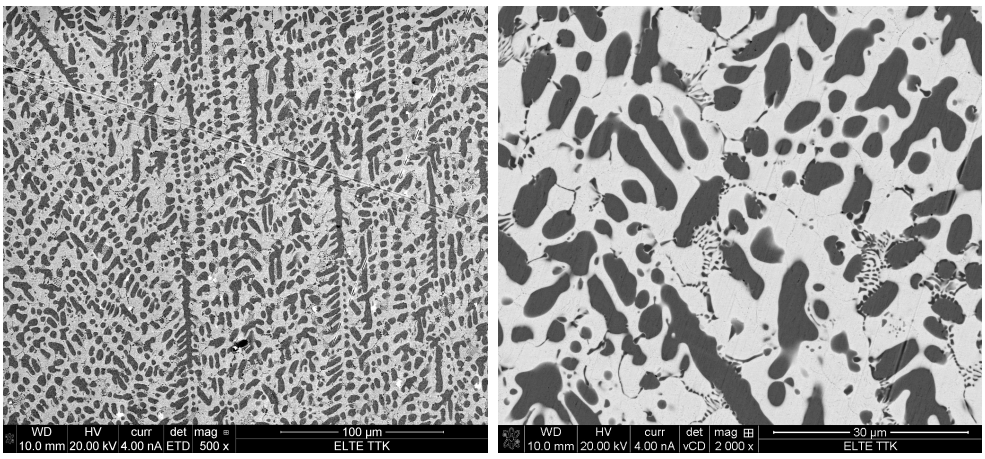

(a) Surface of rm3 (scale bar, 100 μm). **(b)** Phases of rm3 (scale bar, 30 μm).

Figure 4.13: *Snapshots of the surface of rm3, with directional dendrite structure.*

For the element analysis we selected two suitable areas.

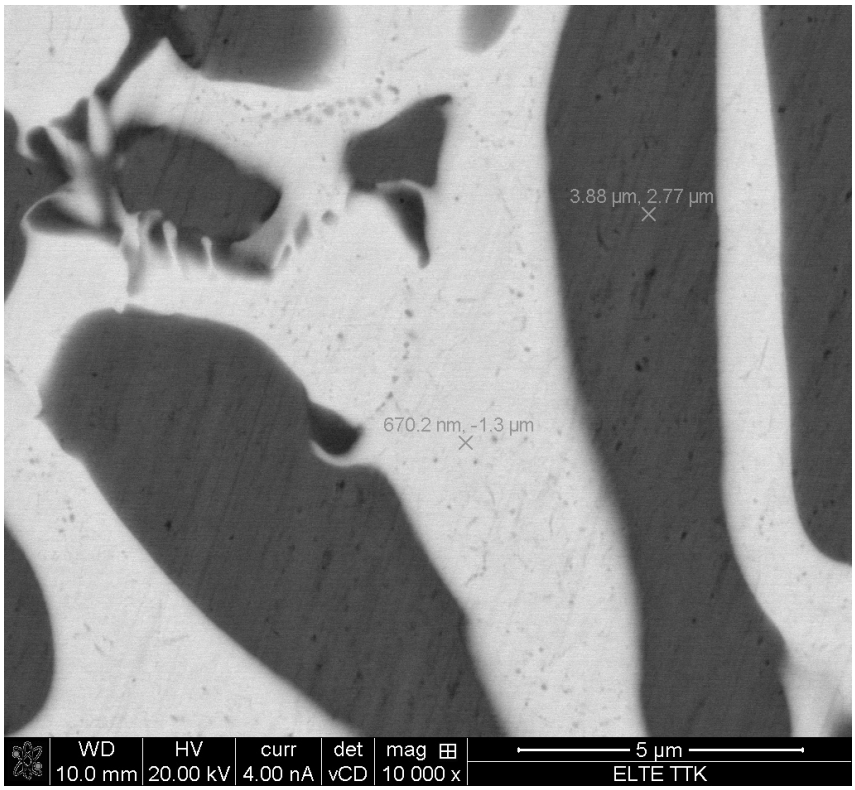

Figure 4.14: *Sampling spots of rm3.*

The result of the analysis is the following:

Element	**Dark [At%]**	**Light [At%]**
Sn	3,14	38,98
Cr	28,37	8,78
Fe	30,24	10,21
Co	27,20	14,00
Ni	11,05	28,03
Total	100	100

Table 4.4: *XRD analysis of the sample rm3.*

The first phase (**Dark**) is almost empty from tin and the nickel is weak against the chromium, iron and cobalt (VEC=7,73) and the second phase (**Light**) is the opposite (VEC=7,74). According to VEC, there is no major crystal structure difference between the phases. We measured two nanoindentation tests on this sample. Based on the results, the elastic modulus is almost the same, and there are two main hardness values for the two phases.

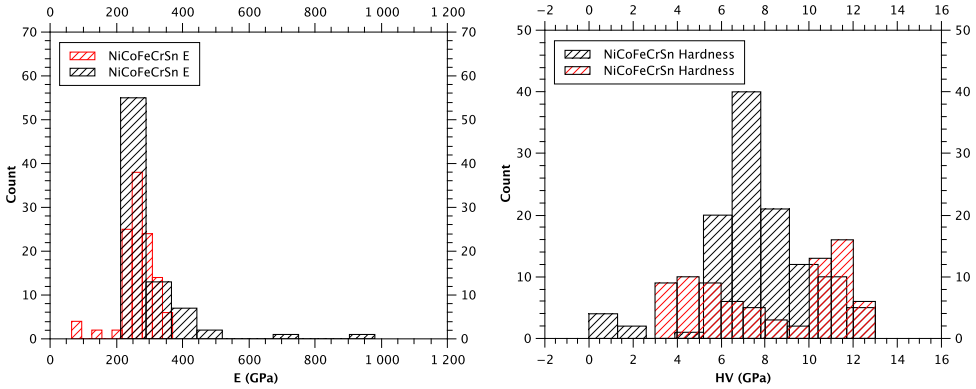

(a) Young's modulus from nanoindentation.

(b) Nano hardness from nanoindentation.

Figure 4.15: *Young's modulus and Nano hardness values from 400 Dynamic Hardness Measurements from two* (200×200) μm *regions, sample rm*3 *(NiCoFeCrSn).*

4.1.5 Alloy rm4 (Ni,Co,Fe,Cr,Ge)

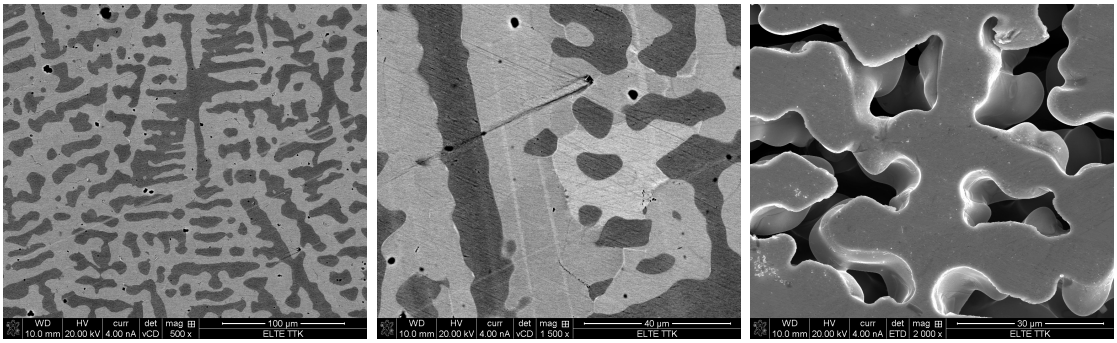

(a) Surface of rm4 (scale bar, 100 μm).

(b) Phases of rm4 (scale bar, 40 μm).

(c) Missing phases of rm4 (scale bar, 30 μm).

Figure 4.16: *Snapshots of the surface of rm4. We can see directional dendrite structure and strange missing phases in the material. In the picture (b) we can see more than two phases. To get some directions about compositions, we did x-ray measurements.*

Element composition of the selected areas:

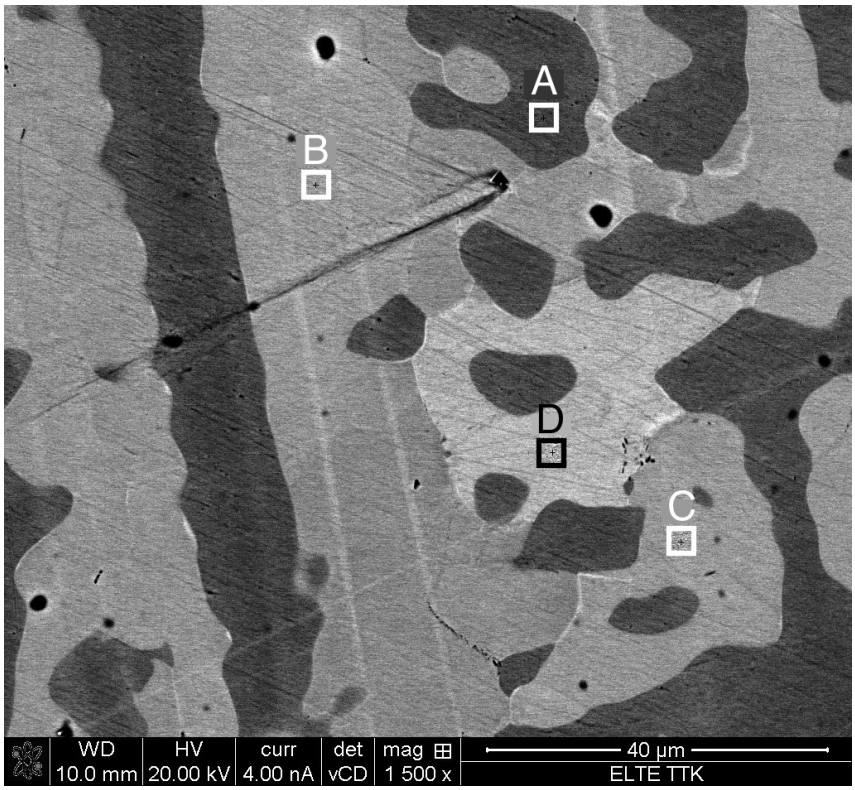

Figure 4.17: *Sampling spots of rm4.*

Element	**A [At%]**	**B [At%]**	**C [At%]**	**D [At%]**
Crl	21,71	18,52	18,61	18,48
Fe	24,37	18,07	18,23	18,22
Co	22,97	18,68	18,79	18,73
Ni	16,62	22,27	22,04	22,00
Ge	14,33	22,45	22,33	22,57
Total	100	100	100	100

Table 4.5: *XRD analysis of the sample rm4.*

Based on the results of EDAX measurements (Tab.4.5), there are just two phases. The B, C, D spots are almost the same. Their phase is weak in chromium, iron and cobalt, but strong in nickel and germanium. The A phase is the opposite. There is partially no difference in the VEC value for the two phases, $VEC_A = 7,57$ and $VEC_{B,C,D} = 7,34$.

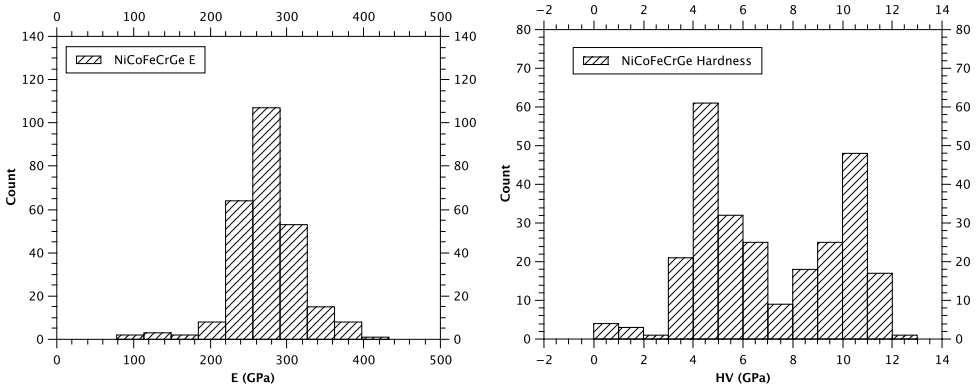

(a) Young's modulus from nanoindentation.

(b) Nano hardness from nanoindentation.

Figure 4.18: *Young's modulus and Nano hardness values from 400 Dynamic Hardness Measurements from* (200×200) μm *region, sample* $rm4$.

4.1.6 Summary

The main results obtained for stainless steel family can be summarized as following:

- Comparing the elastic modulus values obtained from ultrasonic testing and nanoindentation the results can be seen in the following graph (Fig. 4.19).
- It can be seen that the trend between the values obtained by different methods is similar. The results from nanoindentation are much greater than the values obtained from macroscopic measurements. The phenomena is caused by the size-effect, since the hardness and elastic values are sensitive to indentation depth, so the load. In our measurements the maximum used loading was 50 mN.
- Based on our results, the two phased stainless steel HEAs contains one harder and one softer phase in microscopic scale. The macroscopic hardness values act like the microhardness of soft phase, so we can say, that softer phase shall be used as prediction of mechanical properties.
- According to VEC, there was an assumption, that the reference alloy (rmr) is one phased (FCC), and the others are at least two phased materials. As the result of hardness measurements, and based on scanning electron microscopy we got matching results.

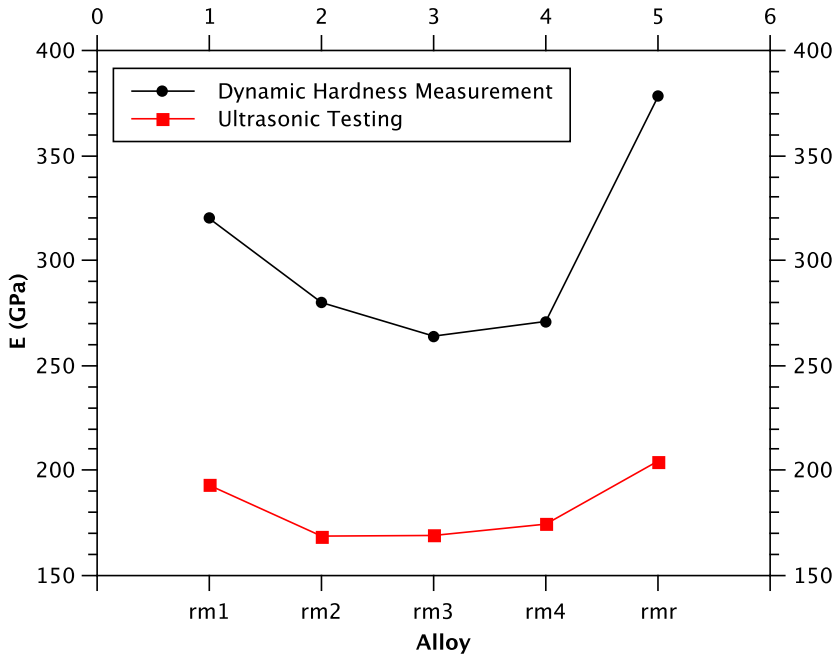

Figure 4.19: *Comparison of elastic modulus obtained from ultrasonic testing and nanoindentation.*

4.2 Refractory HEAs

The refractory HEAs contains Ni, Fe, Cr, Mo, W in different concentration ranges. Compositions made by us are shown in following table

Composition	**Code**	**Calculated density** $[g/cm^3]$	**Experimental density** $[g/cm^3]$
$NiFeCrMoW$	ht1	11,2135	11,2020
$Ni_{38.33}Fe_{36}Cr_{13.88}Mo_{6.66}W_{5.15}$	ht2	9,1261	9,6518
$Ni_{29.5}Fe_{39.8}Cr_{20}Mo_6W_{4.7}$	ht3	8,9053	9,1585
$Ni_{35}Fe_{30}Cr_{20}Mo_{10}W_5$	ht4	9,1148	8,9954

Table 4.6: *Atomic percentages, code names and densities of four refractory HEAs. Two compounds (ht4 and ht1) were investigated during of this thesis.*

Compression. We fabricated our micropillars by Ga focused ion beam. The way of fabrication and investigation is described in the „Experimental methods". Nano compression test were made at room temperature and were performed using linearly increasing force

in time with an instant stop and remove option. According to Hooke's law

$$F = \frac{E_r A}{L} h, \tag{4.1}$$

where E_r is the so-called reduced Young's modulus and it can be determined from the slope of the line fitted to the initial elastic part of stress-strain curves. The A and L are the cross-section and length of the initial cylindrical pillars. When evaluating the results, we observed 2-3 time smaller E values than expected.

Although our samples are policrystalline materials, the fabricated pillars can be regarded as little single crystals, because there are only one or two crystallites in them. Since, the dislocation movement is bounded to slip planes, the applied stress should be high to move them in polycrystalline material. In our case, this movement is much more easier, so called dislocation avalanches can be formed [48]. These avalanches are dislocations moving in parallel slip planes for the same external stress. The strain caused by these avalanches is not as large to see the steps individually, they blend into the linear region of the stress-strain curve, causing smaller slope, then decreasing E values. To receive more reliable results, we should have measure the unloading curve also, where the elastic region is much more accurate. Unfortunately, we did not measured it.

When calculating the elastic modulus of the indented material, beside the contribution of the pillar and the diamond indenter, the deformation of the specimen under the bottom of the pillar has to be also taken into account. During the deformation both the indenter tip and the investigated material deformed also and the measured reduced modulus, E_r contains their common effect as the effect of three elastic bodies being in a serial contact [47].

For this reason a three-term relationship is proposed between the materials Young modulus and the reduced modulus in the following

$$\frac{1}{E_r} = \frac{1-\nu_i^2}{E_i} + \frac{1-\nu^2}{E} + \frac{1-\nu^2}{E} = \frac{1-\nu_i^2}{E_i} + 2\frac{1-\nu^2}{E}, \tag{4.2}$$

where E_i and ν_i are belong to the diamond tip (E_i = 1070 GPa and ν_i =0,17). The second and third terms are correspond by parameters of the HEAs. The Poisson ratio is calculated from ultrasonic tests, thereby E can be calculated.

Alloy: ht4 ($Ni_{35}Fe_{30}Cr_{20}Mo_{10}W_5$)

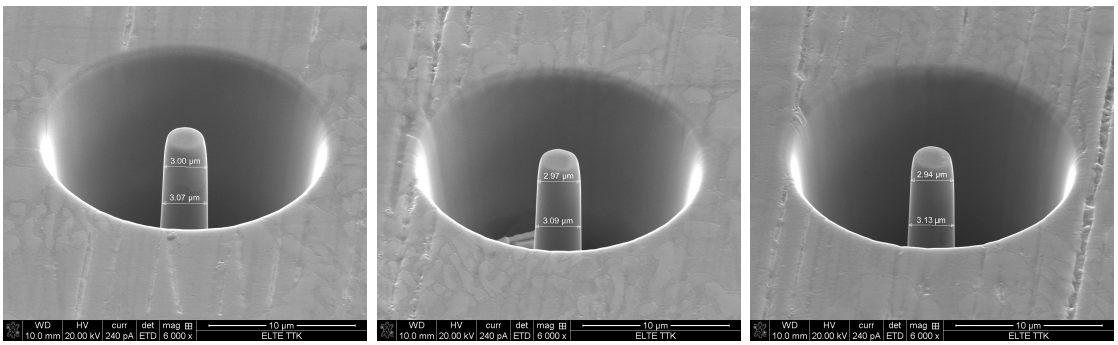

(a) Pillar 1 (scale bar, 10 μm). **(b)** Pillar 2 (scale bar, 10 μm). **(c)** Pillar 3 (scale bar, 10 μm).

Figure 4.20: *Pictures of freshly fabricated micropillars of ht4. After the fabrication we compressed them by loading rate of* $\sim 5 \cdot 10^{-2}$ mN/s.

Lets see the three compressed pillars and their displacement-force curves.

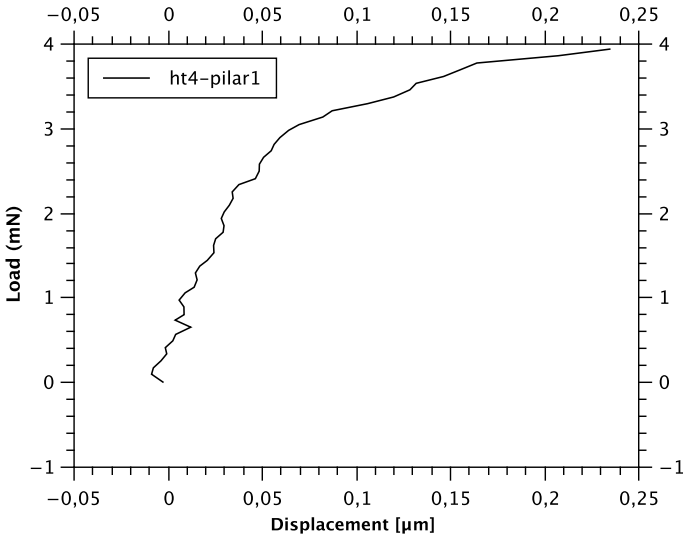

(a) Displacement-force curve of pillar 1.

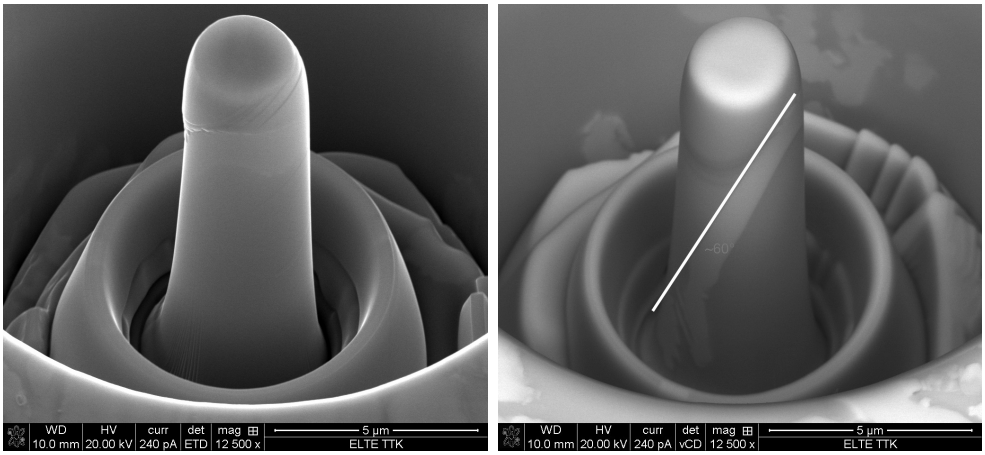

(b) Pillar 1. **(c)** Pillar 1 from another position.

Figure 4.21: *Pictures of first compressed ht4 pillar. In fig (b) we can see the picture of Everhart-Thornley Detector (ETD, for secondary electrons), what is not sensitive to the elements. The snapshot (c) is from another angle with the low Voltage high Contrast Detector (vCD), what is sensitive to elements the electrons come from.*

As we can see, the slip system about 65 degrees activated (indicated in Fig. 4.21(c)) after the critical stress field. The plane might be affected by the different phase what we can see in Fig. 4.21(c). The brighter phase is containing higher tungsten and molybdenum than the other (darker) one. It can be assumed, that the brighter region is much brittle, twith negligible plastic deformation.

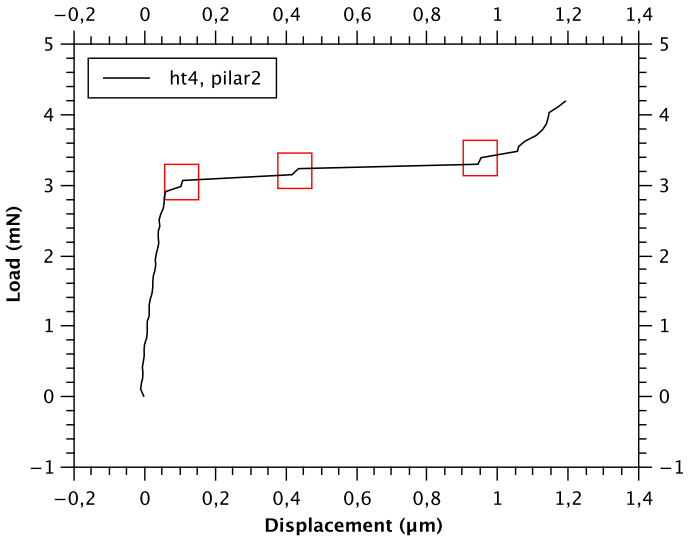

(a) Displacement-force curve of pillar 2.

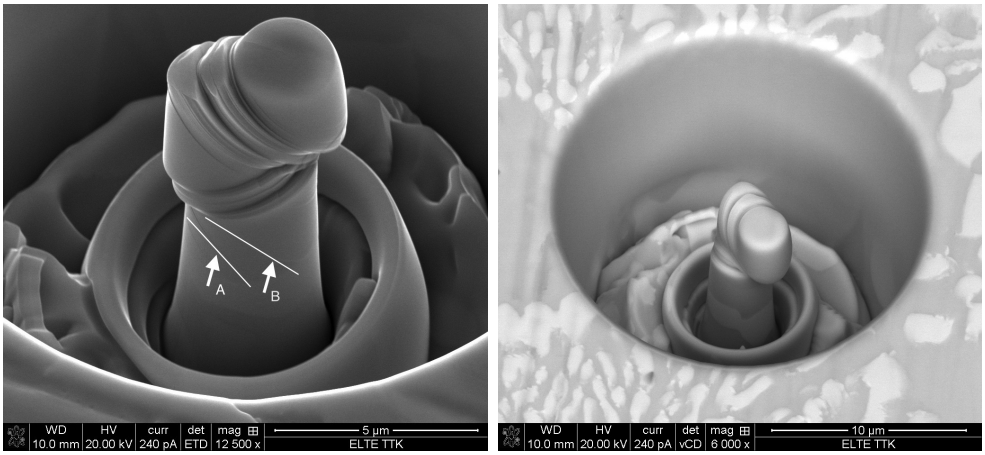

(b) Pillar 2. **(c)** Pillar 2 from another angle.

Figure 4.22: *Pictures of second compressed ht4 pillar, showing the strain-avalanches, which are characterizing the deformations of single crystal pillars.*

After the first slips the indenter reached the virgin part of the pillar, thereby another slip plane could be activated. This behavior can be found also in the force displacement curve (red rectangles). In the picture we can see more planes activating right in the moment of stopping the indentation (A and B arrows in Fig. 4.22(b)).

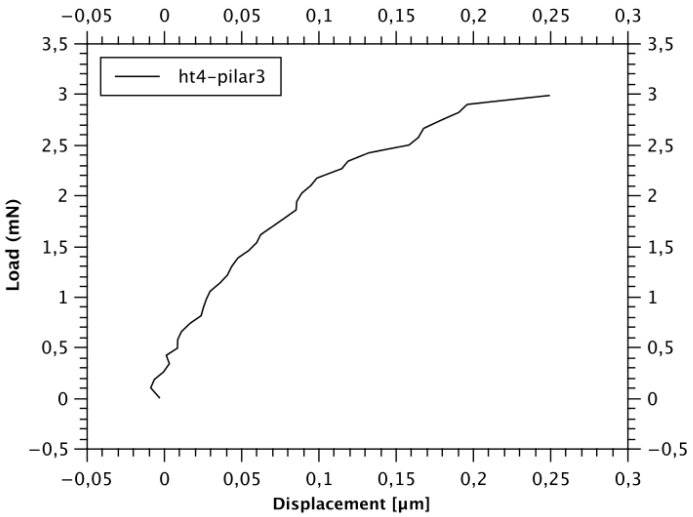

(a) Displacement-force curve of pilar 3.

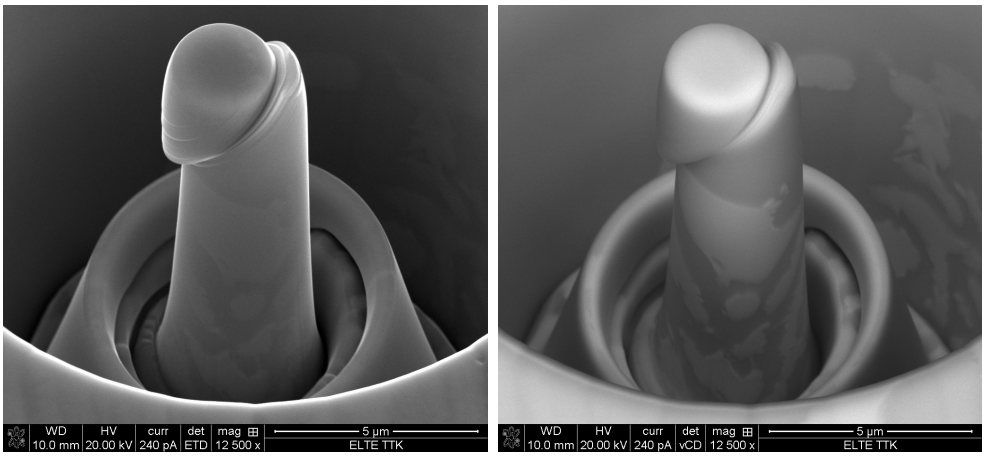

(b) Pilar 3. **(c)** Pilar 3.

Figure 4.23: *Pictures of third compressed ht4 pilar. Here we can see also one slip plane in the darker phase.*

As we mentioned, the bright phase is the brittle one, so the expected BCC. Since, the dislocation movement is more easier in FCC phases (darker) and because of the bottom of the pillar is full of bright areas, only the top of the pillar was deformed.

The calculated stress-strain curves can be seen in the following picture. From the Hooke's law $\sigma = E\varepsilon$, E can be measured from the slope of the initial region of the curves.

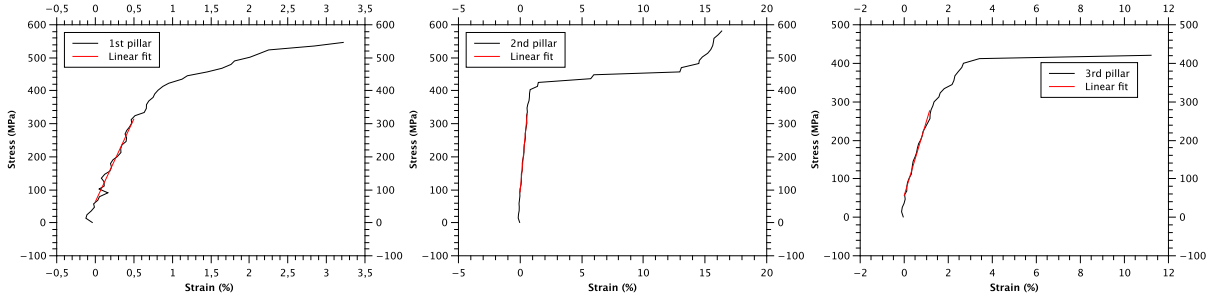

Figure 4.24: *Stress-strain curves for the alloy ht4. The red line indicated is the linear fit, which slope was used for determining the E values.*

As it has been mentioned in the introduction section, the values are lower than expected, what we explained by the existence of dislocation avalanches.The measured E values with errors are plotted to the following graph.

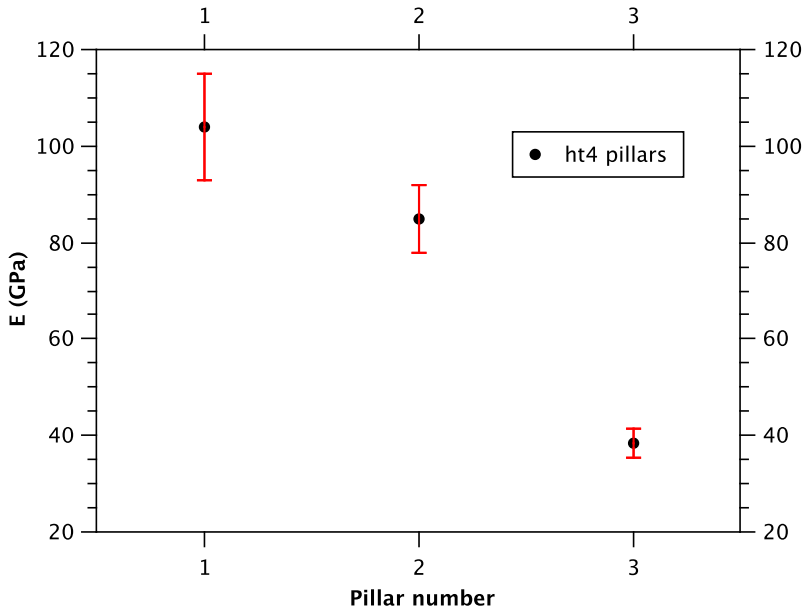

Figure 4.25

The average of values is $E_{avg}^{ht4} = 75,7$ GPa.

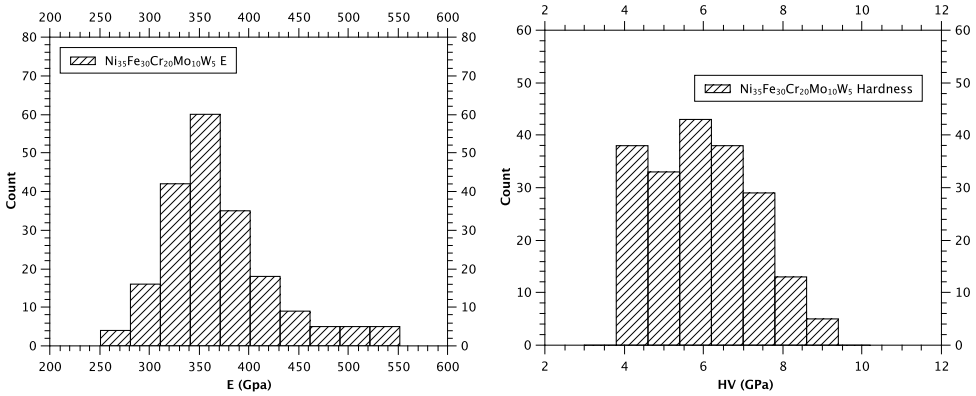

(a) Young's modulus from nanoindentation.

(b) Nano hardness from nanoindentation.

Figure 4.26: *Young's modulus and Nano hardness values from 400 nenoindentation from* (200×200) μm *region, sample ht*4*.*

As we can see (Fig. 4.26) there is only one hardness value obtained from nano measurement, with relatively big error.

Alloy: ht1 ($NiFeCrMoW$)

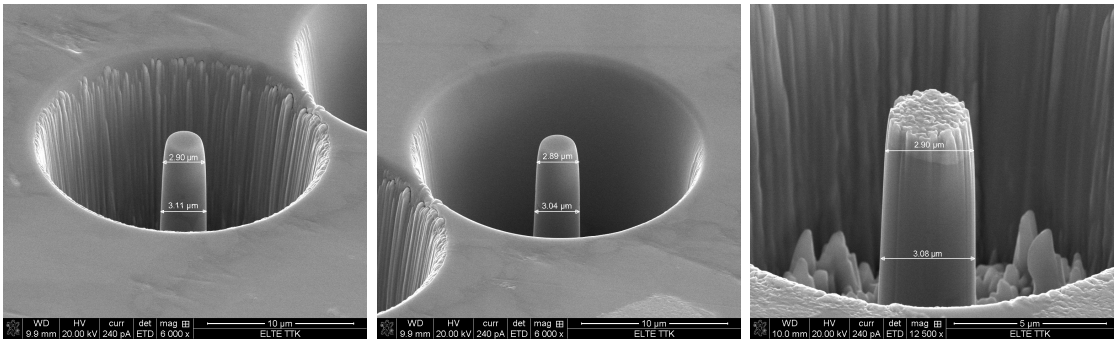

(a) Pilar 1. **(b)** Pilar 2. **(c)** Pilar 3.

Figure 4.27: *Pictures of freshly fabricated micropillars of ht1.*

The top view of the pillars is the following:

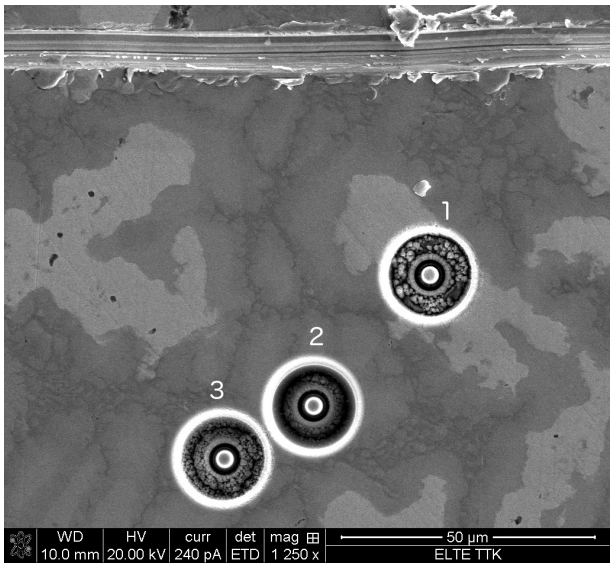

Figure 4.28: *As we can see, we placed the pillars to achieve both dark and bright regions, since they are different in compositions. The brighter region is high in tungsten and molybdenum, the darker is lower of these elements.*

The compression data and their results in pictures are listed in the following pages.

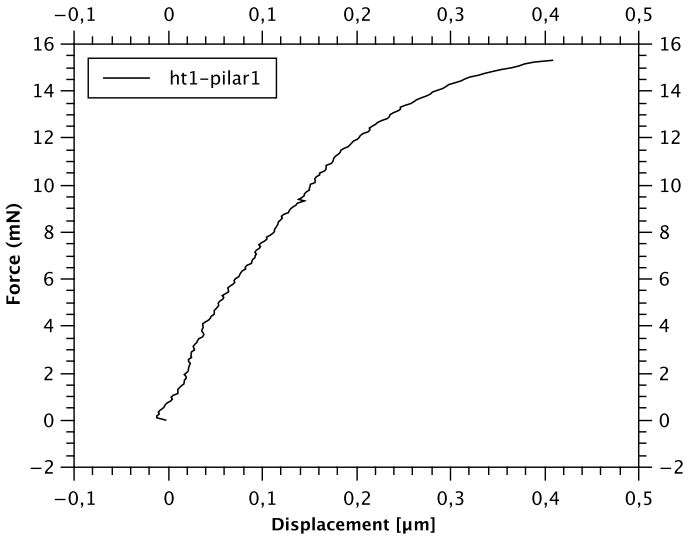

(a) Displacement-force curve of pillar 1. The jump to 10 μm is not shown.

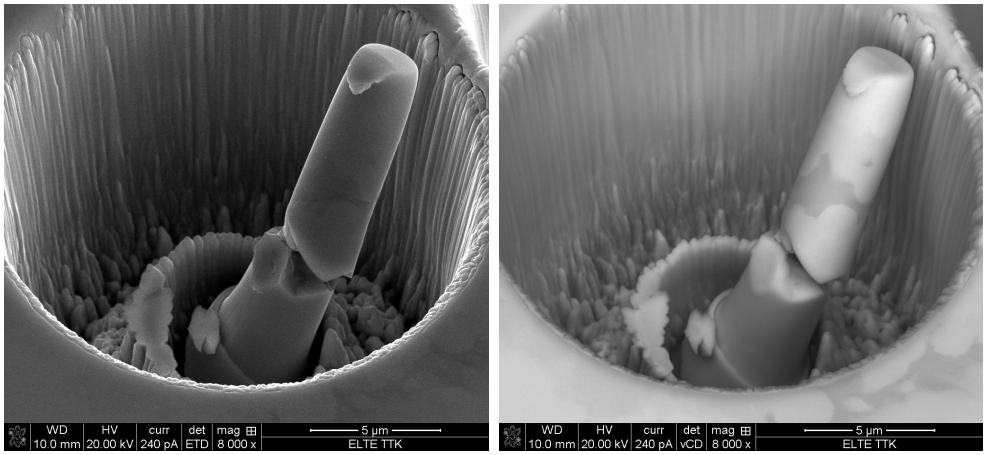

(b) Pillar 1. **(c)** Pillar 1 with another detector.

Figure 4.29: *Pictures of first compressed ht1 pillar. The pillar broke (especially the brighter region, what is supposed to be more brittle than darker) while compression.*

As the Fig. 4.29 (b,c) shows, the placing of indenter was not perfect, the diamond slipped off from the pillar. It is assumed that the crack is right because of this.

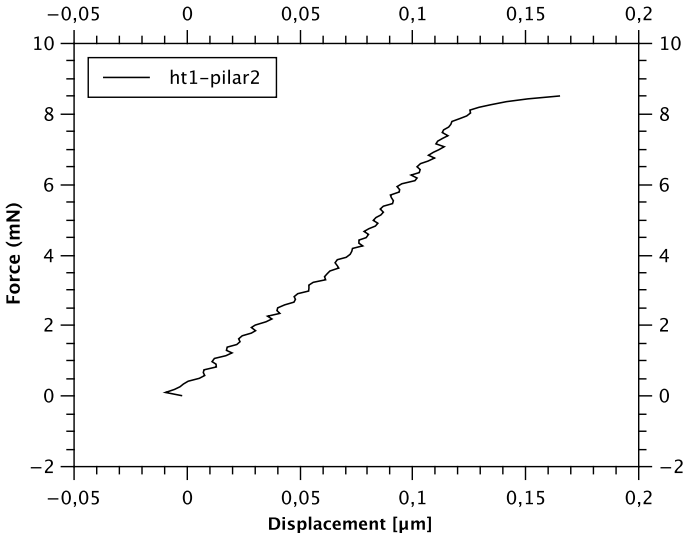

(a) Displacement-force curve of pillar 1.

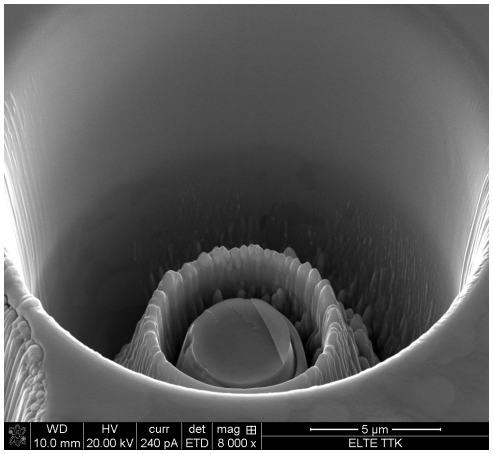

(b) Pillar 2.

Figure 4.30: *The second pillar also shuttered. We have lost this pillar while transporting the specimen from indenter to SEM.*

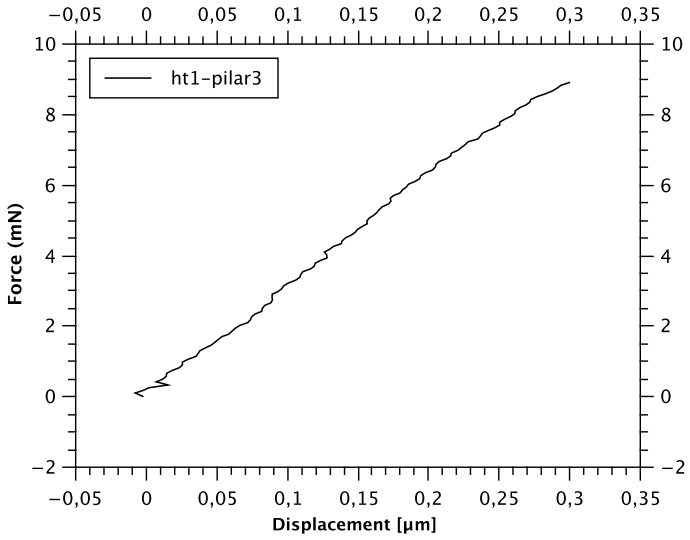

(a) Displacement-force curve of pillar 3.

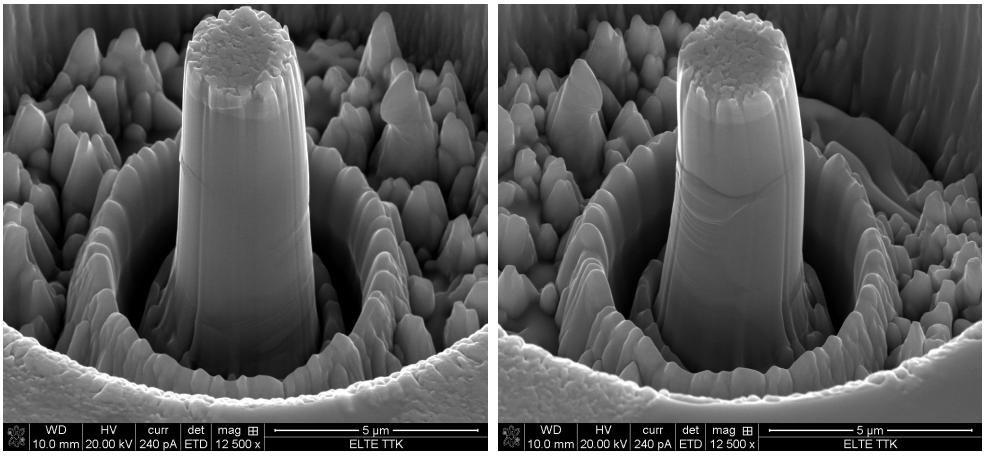

(b) Pillar 3.

(c) Pillar 3.

Figure 4.31: *Snapshots of pillar 3 after compressing. Subfigures (a) and (b) are from different angles.*

Based on the information obtained from SEM and nano indentation, we can say that ht1 is much more brittle than ht4, the ht4 could be easier adapted for everyday use.

The calculated stress-strain curves for this alloy can be seen in the following picture.

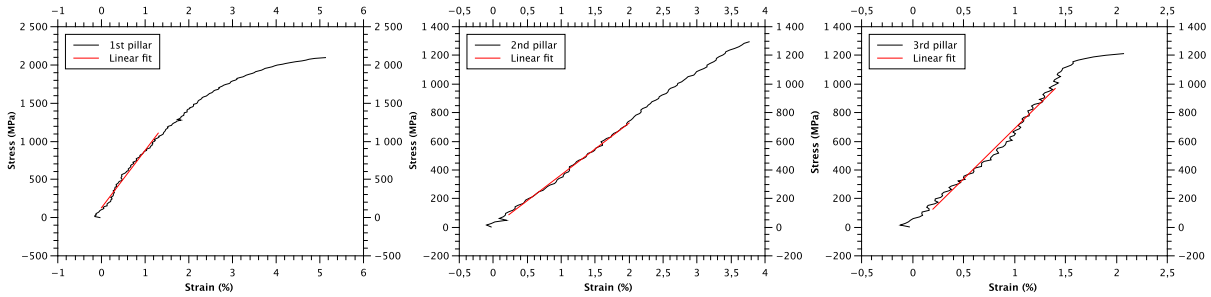

Figure 4.32: *Stress-strain curves for the alloy ht1. The red line indicated is the linear fit, which slope was used for determining the E values.*

As we can see, in the case of ht1 alloy there are much more higher values of E (Fig. 4.32). This was expected from the SEM images and deformation parameters, since the ht1 is more fragile than ht4. The measured E values with errors are plotted to the following graph.

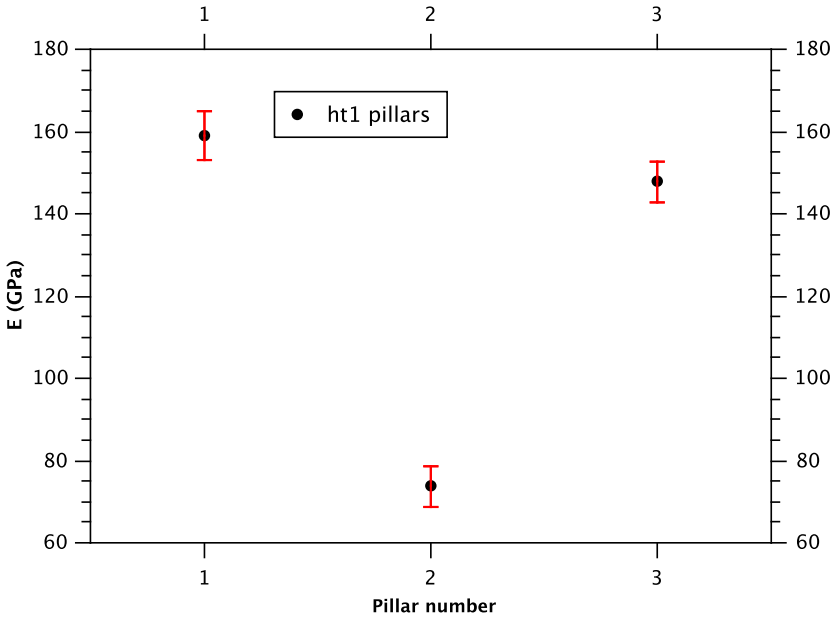

Figure 4.33

The average of values is $E_{avg}^{ht1} = 126,8$ GPa.

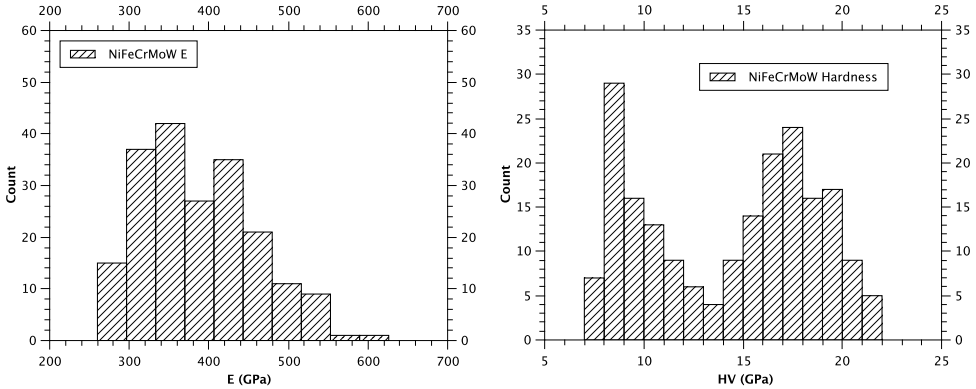

(a) Young's modulus from nanoindentation.

(b) Nano hardness from nanoindentation.

Figure 4.34: *Young's modulus and Nano hardness values from 400 nanoindentations from* (200×200) *µm region, sample ht*1*.*

4.3 Titanium family

The compositions of the samples prepared in this series can be found in Tab. 4.7.

Composition	**Code**	**Calculated density** $[g/cm^3]$	**Experimental density** $[g/cm^3]$
$CuNiCoFeCr$	rez1	8,3357	8,3405
$Cu_xNi_xCo_xFe_xCr_xTi_{1.96}, x = 19.6$	rez2	8,2222	8,2299
$Cu_xNi_xCo_xFe_xCr_xTi_{3.856}, x = 19.23$	rez3	8,1151	8,1500
$Cu_xNi_xCo_xFe_xCr_xTi_{5.66}, x = 18.868$	rez4	8,0144	8,0469
$Cu_xNi_xCo_xFe_xCr_xTi_{7.4}, x = 18,52$	rez5	7,9194	8,0597
$Cu_xNi_xCo_xFe_xCr_xTi_{9.09}, x = 18.18$	rez6	7,8172	7,9703
$Cu_xNi_xCo_xFe_xCr_xTi_x, x = 16.66$	rez7	7,4403	7,6480

Table 4.7: *Atomic percentages, code names and densities of seven titanium family.*

In this family the vickers hardness and the VEC have been compared (Fig. 4.35). One can see, that increasing VEC belongs to lower hardness values. This behavior is well known from the literature, since the lower VEC belongs to brittle but hard BCC and higher VEC to soft, plastically deformable FCC phase.

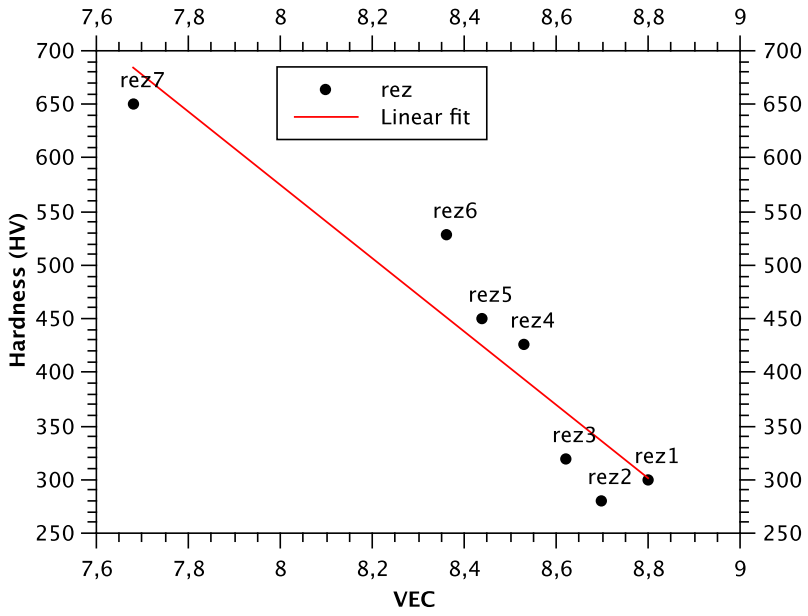

Figure 4.35: *Macroscopic hardness value compared to valence electron concentration.*

We compared the vickers hardness and the shear modulus (G) also.

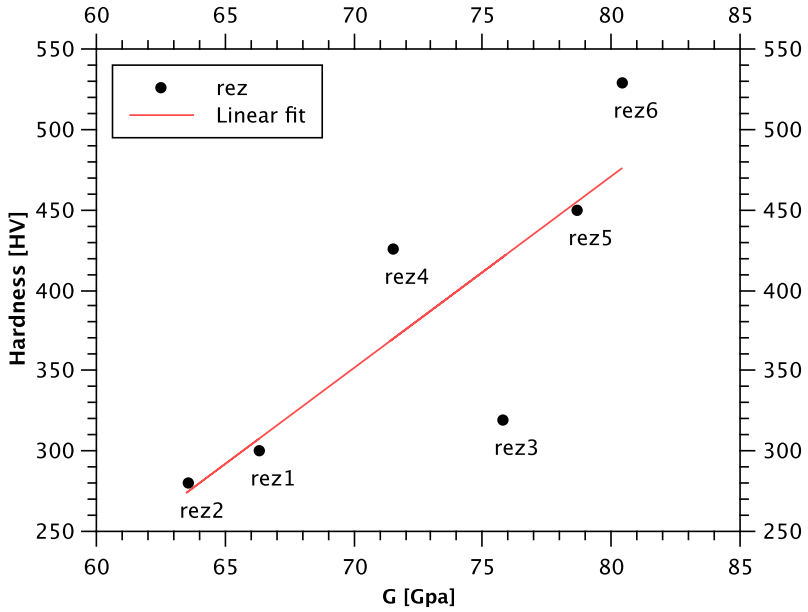

Figure 4.36: *Macroscopic hardness value compared to shear modulus calculated by ultrasonic testing.*

4.4 Aluminum family

Composition	Code	Calculated density $[g/cm^3]$	Experimental density $[g/cm^3]$
$NiCoFeCr$	alu1	8,1823	8,3428
$Ni_xCo_xFe_xCr_xAl_{6.976}, x = 23.255$	alu2	7,0356	7,8111
$Ni_xCo_xFe_xCr_xAl_{11.11}, x = 22.22$	alu3	7,3409	7,1878
$Ni_xCo_xFe_xCr_xAl_x, x = 20$	alu4	6,7243	7,0133
$Ni_xCo_xFe_xCr_xAl_{24.528}, x = 18.867$	alu5	6,4269	6,8608
$Ni_xCo_xFe_xCr_xAl_{27.272}, x = 18.181$	alu6	6,2520	6,6879
$Ni_xCo_xFe_xCr_xAl_{33,36}, x = 16.66$	alu7	6,0815	6,4002

Table 4.8: *Atomic percentages, code names and densities of seven aluminum family.*

We compared the vickers hardness and the VEC. The result is similar like in the case of titanium family.

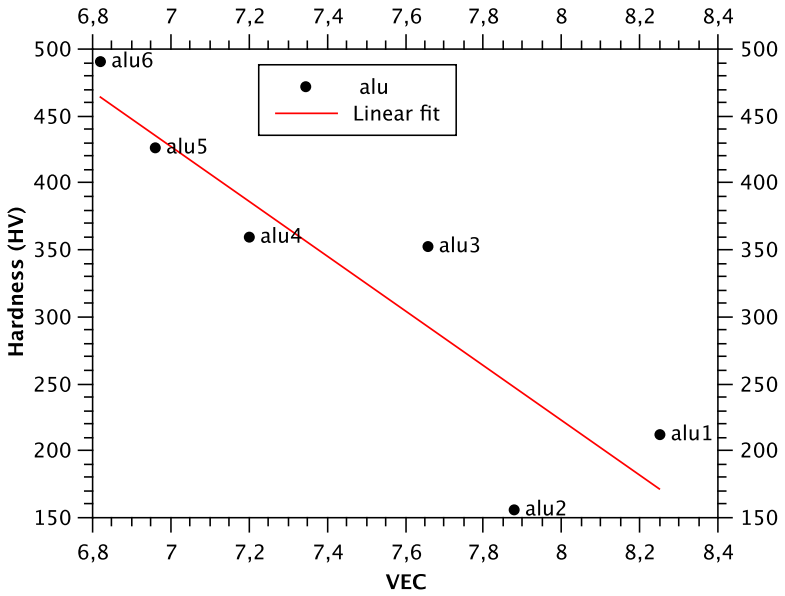

Figure 4.37: *Macroscopic hardness value compared to valence electron concentration.*

Interesting behavior is shown in the hardness-G curve, what is caused by the change in crystalline structure due to the VEC values.

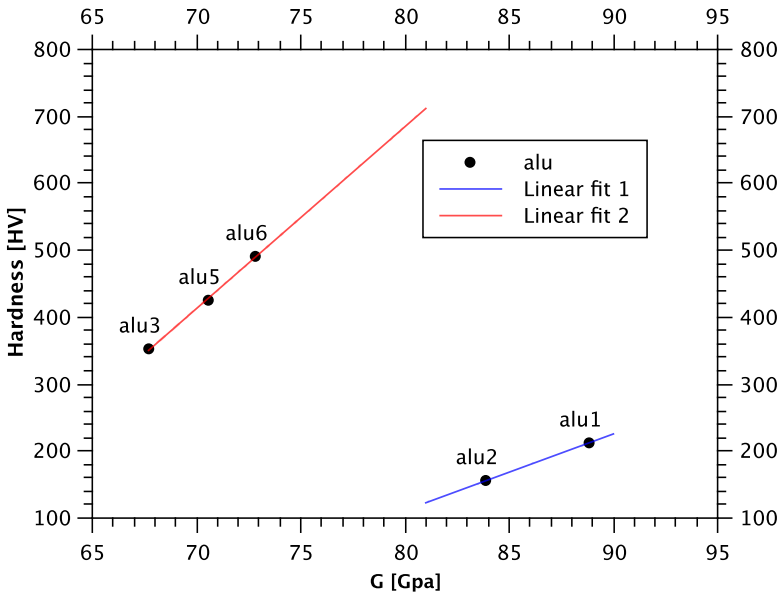

Figure 4.38: *Hardness value compared to shear modulus calculated by ultrasonic testing.*

The *alu*1 is the reference alloy of this family without any aluminum addition and the *alu*2 is very close to *alu*1 in all of properties e.g. (see in the Summary chapter). The change in crystalline structure occurs from alloy *alu*3 and this is the reason, why we can see detachment in this plot (Fig. 4.38).

4.5 Density measurement

Figure 4.39 shows the experimentally determined density in the function of calculated value for all investigated alloys. Since there are many compounds in one sample (at least 4 but there can be 6 also), the computation is cumbersome. Calculation method from Dávid Molnár's thesis [1] is the following:

$$\bar{\rho} = \frac{\sum_i c_i m_i}{\sum_i c_i V_i}, \tag{4.3}$$

where $\bar{\rho}$ is the average concentration, c_i the atomic concentrations of alloying elements, m_i is the molar mass in g/mol and V_i is the volume of Wigner-Seitz (WS) cell in cm^3. The molar volume V_i is calculated by Eq. 4.4 by using WS radius obtained by *ab initio* calculations [1]

$$V = \frac{4}{3}\pi w^3 \cdot N_A, \tag{4.4}$$

where w is the radius of the WS cell and N_A is the Avogadro number.

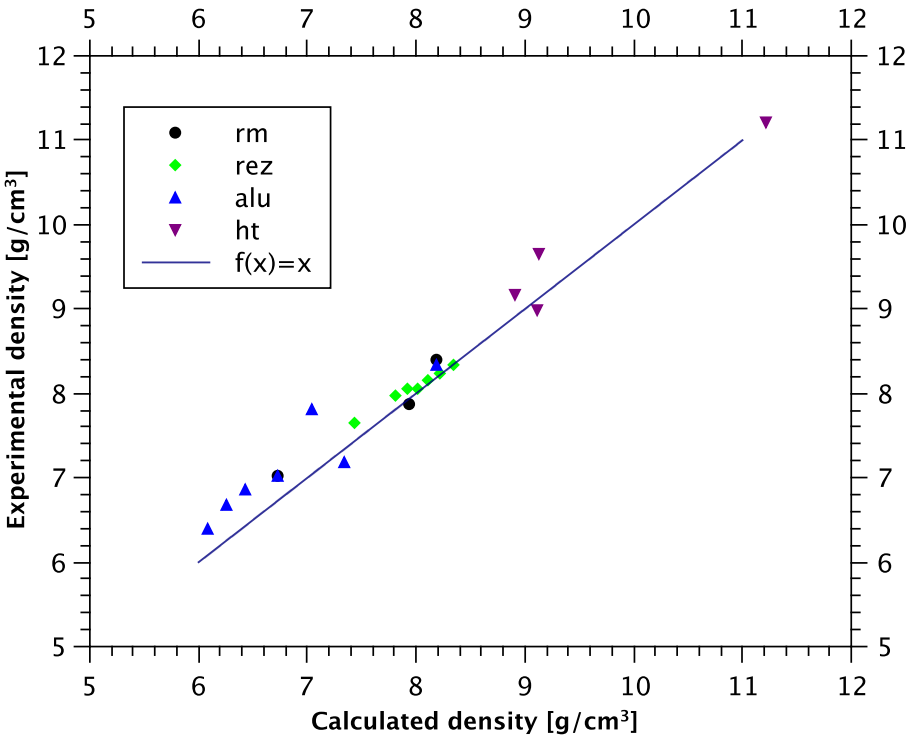

Figure 4.39: *Graph of calculated and measured densities of our HEAs.*

In general the experimental data are above the calculated ones indicating shrinkage of the structure despite of its disordered nature. It should be mentioned that in the case of single-phase alloys the measured and calculated data lays on the first bisector and the measured data for two-phases are higher in density compared to the calculated ones.

Chapter 5

Summary

Stainless steel based HEAs ($NiCoFeCr\ SP_x$, where $SP_x = Al, Ga, Ge, Sn$, marked with $rm_{r,1,...,4}$).

The VEC values for HEAs with *sp* additions are between 7.2-7.4 which predict [32] two phase nature in accordance with the experimental findings, except the reference alloy (VEC=8.3).
Addition of these *sp* elements hardens the reference alloy. Addition of *Al* and *Sn* makes the initial alloy more harder than the addition of *Ga* and *Ge*. All of the members of this family seemed to be useful for high strength applications due to their high hardness linked with relatively high ductility.
Interesting to mention that all these stainless steel based HEAs with *sp* additions were found to be ferromagnetic which is probably connected with their two-phase nature. The two phase nature was revealed also by nanoindentation method.

Refractory HEAs ($NiFeCrMoW$, marked with $ht_{1,2}$).

Out of 4 inductively melted refractory HEAs only 2 have been investigated so far. These were found two-phase materials. The alloy with equimolar composition ($ht1$) was found extremely hard (600 HV) probably due to the high wolfram and molybdenum content. These high strength HEAs will be further investigated (corrosion, oxidation and wear resistance measurements).

Titanium family ($CuNiCoFeCrTi_y$), marked as $rez_{1,2,...,7}$.

For this single phase family of HEAs we could almost double the hardness (which is proportional to strength) with only 9 percentage of Ti, whereas the bulk modulus decreased from 176 to 138 GPa and the Young modulus slightly increased from 176 to 205 GPa. The shear modulus was found to be almost constant (see Fig. 5.1). Unfortunately the increase of hardness was found to be connected to the increase of brittleness which makes this family not practical for industrial use. This family was found to be nonmagnetic.

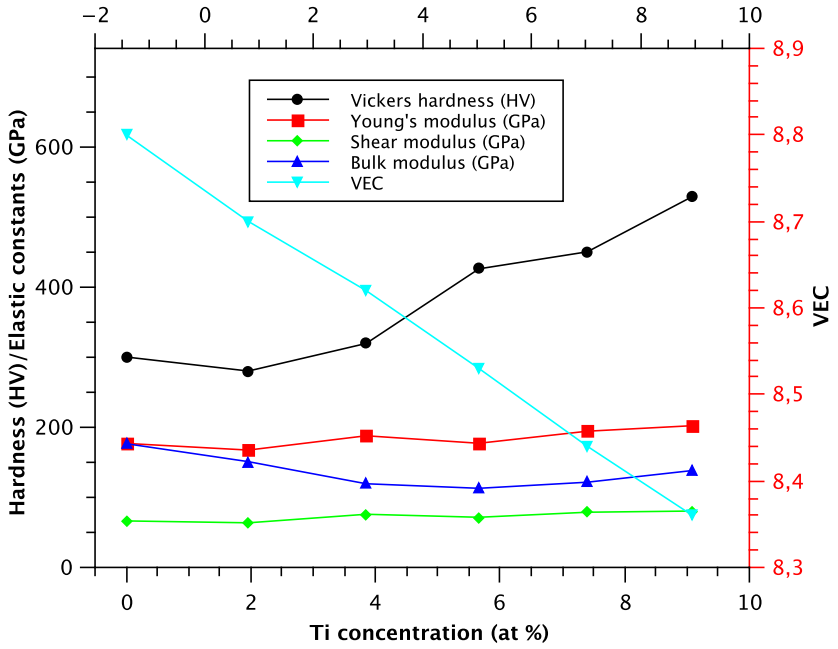

Figure 5.1: *Hardness and elastic properties in the function of titanium content.*

Aluminum family ($NiCoFeCrAl_y$), marked $alu_{1,2,...,7}$.

In this family only the first two (alu_1, alu_2 with small Al concentration) was found single phase material. The more than 2.5 $\times$ increase of hardness with increasing Al concentration is connected to the cocktail effect of the two phases present in high Al content alloys (see Fig. 5.2).

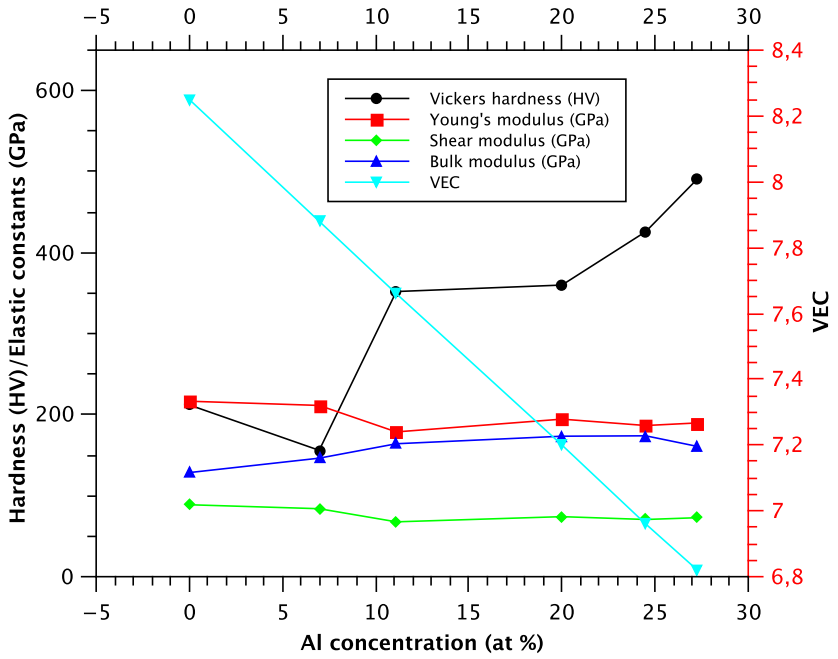

Figure 5.2: *Hardness and elastic properties in the function of aluminum content.*

Interestingly the bulk modulus slightly increased and the Young modulus slightly decreased as a function of aluminum content, which is just an opposite behavior compared with the titanium based HEAs. This tendency of the mechanical properties needs further investigations.

Chapter 6

Future tasks

As usually it happens, we have got more questions than answers during our investigations. To get the answers we have to solve some tasks in the future:

High temperature hardness measurement. Since we are seeking for a HEA composition for high temperature applications, we have to build an instrument, what is able to measure the hardness in the 1000-1300°C temperature range.

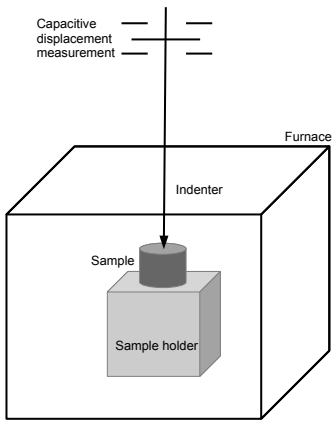

Figure 6.1: *Schematics for high temperature indenter.*

The device is under construction. The conception is to measure the displacement of the wolfram tip under a constant load. The indentation depth will be measured in the function of time and temperature.

Thermal dilatation measurements. Up to our knowledge, such data are missing in the literature, although they are strongly needed for our theoretical partners in their *ab initio* calculations. We intend to perform these measurements within our collaboration with the Transilvania University Brasov, Romania, where the thermal dilatation measurements can be performed with Linseis L75/230 (Germany) instrument.

Tensile stress-strain measurements. In the literature we can find large number of compression tests and micropillar deformation measurements, but only a few a tensile and bending tests. The compression test is relative easy to perform and needs a small sample (for example parallel prism 3 by 3 by 6 mm). We prepared samples for tensile stress-strain measurements from our inductively ingots by spark erosion cutting having size shown in the Fig. 6.2(a).

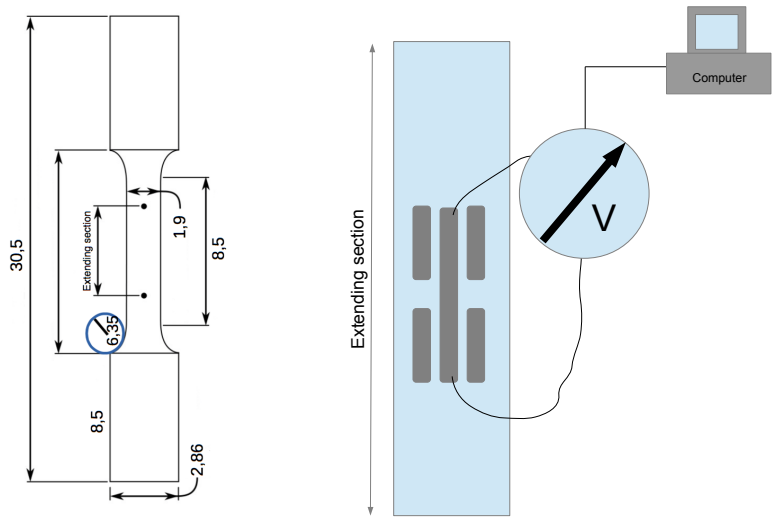

(a) Reduced ASTM A8 sample.

(b) Strain gauge.

Figure 6.2: *Diagram of reduced sample and orientation of strain gauge.*

Unfortunately the strain measurement 100 kN testing machine (United Test, China) is not sufficient for such a small sample. This is why we use strain gauge shown in the Fig. 6.2(b) to increase the precision and resolution of the measurements.

Budapest, 29th of May, 2015.

Bibliography

[1] Dávid S. Molnár, Investigation of the properties of high entropy alloys by ab initio calculations, Master's thesis (2015, ELTE).

[2] Cantor, B., 2007. Stable and metastable multicomponent alloys. Ann. Chim. Sci. Mat. 32, 245-256.

[3] Yeh, J.W., Chen, S.K., Gan, J.Y., Lin, S.J., Chin, T.S., Shun, T.T., et al., 2004a. Formation of simple crystal structures in $CuCoNiCrAlFeTiV$ alloys with multiprincipal metallic elements. Metall. Mater. Trans. A 35

[4] Yeh, J.W., 2006. Recent progress in high-entropy alloys. Ann. Chim. Sci. Mat. 31, 633-648.

[5] B. S. Murphy, Jien-Wei Yeh, S. Ranganathan, High Entropy Alloys, Book, 2014

[6] Lu, Y et al. A promising new class of high-temperature alloys. eutectic high entropy alloys, Sci. Rep. 4, 6200. DOI:10.1038/srep06200 (2014)

[7] Ming-Hung Tsai and Jien-Wei Yeh (2014) High-Entropy Alloys: A Critical Review, Materials Research Letters, 2:3, 107-123, DOI: 10.1080/21663831.2014.912690

[8] Yeh, J.W., 2006. Recent progress in high-entropy alloys. Ann. Chim. Sci. Mat. 31, 633-648.

[9] Fultz, B., 2010. Vibrational thermodynamics of materials. Prog. Mater Sci. 55, 247-352.

[10] Swalin, R.A., 1972. Thermodynamics of Solids. John Wiley and Sons, Toronto.

[11] Yeh, J.W., 2013b. Future trends of high-entropy alloys. High-Value Metals Forum, MRS-T Annual Meeting-2013, Jhongli, Taiwan.

[12] Takeuchi, A., Inoue, A., 2000. Calculations of mixing enthalpy and mismatch entropy for ternary amorphous alloys. Mater. Trans. 41, 1372-1378.

[13] Cullity, B.D., Stock, S.R., 2001. Elements of X-Ray Diffraction. Prentice Hall, New Jersey, USA.

[14] Reed-Hill, R.E., Abbaschian, R., 1994. Physical Metallurgy Principles. PWS Publishing, Boston, USA.

[15] Porter, D.A., Easterling, K.E., 1992. Phase Transformations in Metals and Alloys. CRC Press, London, UK.

[16] Massalski, T.B., 1989. Phase diagrams in materials science. Metall. Trans. A 20A, 1295-1323.

[17] Pettifor, D.G., 1996. Phenomenology and theory in structural prediction. J. Phase Equilib. 17, 384-399.

[18] de Graef, M.D., McHenry, M.E., 2012. Structure of Materials: An introduction to Crystallography, Diffraction and Symmetry. Cambridge University Press, Cambridge, UK.

[19] Senkov, O.N., Wilks, G.B., Miracle, D.B., Chuang, C.P., Liaw, P.K., 2010. Refractory high- entropy alloys. Intermetallics 18, 1758-1765.

[20] Tsai, K.Y., Tsai, M.H., Yeh, J.W., 2013b. Sluggish diffusion in $CoCrFeMnNi$ high-entropy alloys. Acta Mater. 61

[21] Yeh JW, Chen SK, Lin SJ, Gan JY, Chin TS, Shun TT, Tsau CH, Chang SY. Nanostructured high-entropy alloys with multiple principal elements: novel alloy design concepts and outcomes. Adv Eng Mater. 2004;6:299–303.

[22] Tong et al., Microstructure character- ization of AlxCoCrCuFeNi high-entropy alloy system with multiprincipal elements. Metall Mater Trans A. 2005;36:881–893.

[23] Hsu CY, Yeh JW, Chen SK, Shun TT. Wear resis- tance and high-temperature compression strength of Fcc CuCoNiCrAl0.5 Fe alloy with boron addition. Metall Mater Trans A. 2004;35:1465–1469.

[24] Zhang KB, Fu ZY. Effects of annealing treat- ment on phase composition and microstructure of CoCrFeNiTiAlx high-entropy alloys. Intermetallics. 2012;22:24–32.

[25] Tsai MH, Yeh JW, Gan JY. Diffusion barrier prop- erties of AlMoNbSiTaTiVZr high-entropy alloy layer between copper and silicon. Thin Solid Films. 2008;516: 5527–5530.

[26] Tsai MH, Wang CW, Tsai CW, Shen WJ, Yeh JW, Gan JY, Wu WW. Thermal stability and performance of NbSiTa- TiZr high-entropy alloy barrier for copper metallization. J Electrochem Soc. 2011;158:H1161–H1165.

[27] Otto F, Yang Y, Bei H, George EP. Relative effects of enthalpy and entropy on the phase stability of equiatomic high-entropy alloys. Acta Mater. 2013;61: 2628–2638.

[28] Lin CW, Tsai MH, Tsai CW, Yeh JW, Chen SK. Microstructure and aging behavior of Al5 Cr32 Fe35 Ni22 Ti6 ternary-like high-entropy alloy. In preparation.

[29] Cheng KH, Lai CH, Lin SJ, Yeh JW. Recent progress in multi-element alloy and nitride coatings sputtered from high-entropy alloy targets. Ann Chim-Sci Mat. 2006;31:723–736.

[30] Chen YY, Duval T, Hong UT, Yeh JW, Shih HC, Wang LH, Oung JC. Corrosion properties ofa novel bulk Cu0.5NiAlCoCrFeSi glassy alloy in 288 C high-purity water. Mater Lett 2007;61:2692–2696.

[31] Singh S, Wanderka N, Murty BS, Glatzel U, Ban- hart J. Decomposition in multi-component AlCoCr- CuFeNi high-entropy alloy. Acta Mater. 2011;59: 182–190.

[32] Tian, F., Varga, L. K., Chen, N., Delczeg, L. and Vitos, L. Ab initio investigation of high-entropy alloys of 3d elements. Phys. Rev. B 87, 075144 (2013).

[33] Senkov ON, Scott JM, Senkova SV, Miracle DB, Wood- ward CF. Microstructure and room temperature prop- erties of a high-entropy TaNbHfZrTi alloy. J Alloys Compd. 2011;509:6043–6048.

[34] Tung CC, Yeh JW, Shun TT, Chen SK, Huang YS, Chen HC. On the elemental effect of AlCoCrCuFeNi high-entropy alloy system. Mater Lett. 2007;61:1–5.

[35] Guo S, Ng C, Lu J, Liu CT. Effect of valence electron concentration on stability of fcc or bcc phase in high entropy alloys. J Appl Phys. 2011;109:103505.

[36] Wen LH, Kou HC, Li JS, Chang H, Xue XY, Zhou L. Effect of aging temperature on microstructure and properties of AlCoCrCuFeNi high-entropy alloy. Inter- metallics. 2009;17:266–269.

[37] Tsai CW, Chen YL, Tsai MH, Yeh JW, Shun TT, Chen SK. Deformation and annealing behaviors of high-entropy alloy Al0.5 CoCrCuFeNi. J Alloys Compd. 2009;486:427–435.

[38] Shun TT, Du YC. Microstructure and tensile behav- iors of FCC Al0.3CoCrFeNi high entropy alloy. J Alloys Compd. 2009;479:157–160.

[39] Wang WR, Wang WL, Wang SC, Tsai YC, Lai CH, Yeh JW. Effects of Al addition on the microstructure and mechanical property of Alx CoCrFeNi high-entropy alloys. Intermetallics. 2012;26:44–51.

[40] Kao YF, Chen TJ, Chen SK, Yeh JW. Microstruc- ture and mechanical property of as-cast, -homogenized, and -deformed AlxCoCrFeNi ($0 \leq x \leq 2$) high-entropy alloys. J Alloys Compd. 2009;488:57–64.

[41] Li C, Li JC, Zhao M, Jiang Q. Effect of aluminum con- tents on microstructure and properties of AlxCoCrFeNi alloys. J Alloys Compd. 2010;504:S515–S518.

[42] Lin CM, Tsai HL. Evolution of microstructure, hardness, and corrosion properties of high-entropy Al0.5 CoCrFeNi alloy. Intermetallics. 2011;19:288–294.

[43] Senkov ON, Wilks GB, Scott JM, Miracle DB. Mechani- cal properties of Nb25 Mo25 Ta25 W25 and V20 Nb20 Mo20 Ta20 W20 refractory high entropy alloys. Intermetallics. 2011;19:698–706.

[44] Yang X, Zhang Y, Liaw PK. Microstructure and com- pressive properties of NbTiV-TaAlx high entropy alloys. Procedia Eng. 2012;36:292–298.

[45] Microstructure and Properties of Aluminum-Containing Refractory High-Entropy Alloys, O.N. SENKOV, C. WOODWARD, and D.B. MIRACLE, JOM, Vol. 66, No. 10, 2014, pages: 2030-2042

[46] Santodonato, L. J. et al. Deviation from high-entropy config- urations in the atomic distributions of a multi-principal-element alloy. Nat. Commun. 6:5964 doi: 10.1038/n-comms6964 (2015).

[47] Tamás Csanádi, M. Blanda, A. Duszova, N.Q. Chinh, P. Szommer, J. Dusza, Deformation characteristics of WC micropillars, Journal of Europen Ceramic Society, 2014

[48] Dennis M. Dimiduk,Chris Woodward, Richard LeSar, Michael D. Uchic, Scale-Free Intermittent Flow in Crystal Plasticity, SCIENCE VOL 312 26 MAY 2006

[49] Nanoméretű minták deformációs tulajdonságainak vizsgálata – Hegyi Ádám István - Fizika Bsc szakdolgozat, ELTE TTK, 2011

[50] Davis, Joseph R. (2004). Tensile testing (2nd ed.). ASM International. ISBN 978-0-87170-806-9.

[51] W.M. Haynes, CRC Handbook of Chemistry and Physics, 94th Edition, CEC Press

[52] "Bragg diffraction 2" by Hydrargyrum - Own work. Licensed under CC BY-SA 3.0 via Wikimedia Commons

NYILATKOZAT

Név: Vida Ádám

ELTE Természettudományi Kar, szak: Anyagtudomány MSc

ETR azonosító: IKHRWM

Diplomamunka címe:
Preparation and investigation of high entropy alloys.

A **diplomamunka** szerzőjeként fegyelmi felelősségem tudatában kijelentem, hogy a dolgozatom önálló munkám eredménye, saját szellemi termékem, abban a hivatkozások és idézések standard szabályait következetesen alkalmaztam, mások által írt részeket a megfelelő idézés nélkül nem használtam fel.

Budapest, 2015.05.29.

_____

a hallgató aláírása